Available online at www.sciencedirect.com
SCIENCE DIRECT
ELSEVIER
Lithos 88 (2006) 201–232
LITHOS
www.elsevier.com/locate/lithos

Temperature–time paths from phosphate accessory phase paragenesis in the Honey Brook Upland and associated cover sequence, SE Pennsylvania, USA

Joseph M. Pyle

Department of Earth and Environmental Sciences, Rensselaer Polytechnic Institute, Troy, NY, 12180-3522, USA

Received 14 February 2005; accepted 16 August 2005
Available online 19 December 2005

Abstract

Analysis of monazite-bearing lithologies from the Precambrian Honey Brook Upland (HBU) and overlying metasedimentary Paleozoic Chester Valley Sequence (CVS) (SE PA, USA) reveals overprinting of primary major and accessory phase parageneses by texturally and compositionally disparate secondary accessory phase parageneses. Two-pyroxene temperatures of 915–945 °C for reconstituted pyroxene reflect emplacement temperatures of felsic plutonic rocks (opdalite, charnockite) prior to Mesoproterozoic metamorphism. Monazite in metavolcanic felsic gneiss yields three age domains at 1009 ± 4 Ma (2 s.e.), 965 ± 6, and 876 ± 10 Ma. The first two domains record metamorphism of the HBU after anorthosite intrusion; peak monazite–xenotime temperatures for the monazite core domain are ~700 °C, and high Th/U values in the second (overgrowth) age domain likely reflect a second high-*T* monazite growth episode. Formation of cummingtonite coronas on orthopyroxene in opdalite constrains maximum ~1010 Ma metamorphic temperatures in the "granulite-facies" terrane to 730–740 °C. Evidence of increased Cl fluid activity in the ~965 Ma metamorphism includes higher Cl content of matrix apatite relative to garnet-included apatite (metavolcanics), and Cl-bearing K-hornblende succeeding cummingtonite in coronal overgrowths (opdalite). Extreme monazite Th/U values (75–250) in the rim domain suggest growth during low-*T* hydrothermal alteration. In the opdalite, secondary singe-grain monazite and monazite + xenotime metasomites in apatite yield ages of 714 ± 24 and 586 ± 88 Ma, temperatures of 325–425 °C, and are interpreted to reflect thermal disturbances associated with late Proterozoic plutonic and volcanic activity in the Upland. This thermal disturbance may be recorded by Rb–Sr age of 567 Ma for biotite from a HBU gneiss. Monazite age domains in metaquartzite (378 ± 28, 272 ± 44 Ma) suggest that low-grade metamorphism (260–320 °C, Mnz–Xno thermometry) of the CVS is not a result of Taconian orogenesis.

Keywords: Monazite; Electron microprobe; Geothermometry; Grenville orogeny; Pennsylvania Piedmont

1. Introduction

Utilization of phosphate accessory phases as combined geochronometers and geothermometers yields discrete *T–t* points for polymetamorphosed rocks, as well as for monocyclic metamorphic rocks, if the phosphates undergo multiple growth reactions over the duration of a single *P–T* loop (e.g., Pyle and Spear, 2003; Pyle et al., 2005). Both monazite and xenotime are dateable by isotopic U–Pb (e.g., Parrish, 1990), Th–Pb (Harrison et al., 1995) and derivative Pb–Pb methods, as well as U–Th–total Pb chemical (electron microprobe) methods (e.g., Montel et al., 1996). Growth or equilibration temperatures are retrievable through application of phosphate geothermometers to equilibrat-

E-mail address: pylej@rpi.edu.

0024-4937/$ - see front matter © 2005 Elsevier B.V. All rights reserved.
doi:10.1016/j.lithos.2005.08.010

ed monazite–xenotime (Gratz and Heinrich, 1997; Heinrich et al., 1997; Pyle et al., 2001; Seydoux-Guillaume et al., 2002), xenotime–garnet (Pyle and Spear, 2000), or monazite–garnet (Pyle et al., 2001) mineral pairs.

The aim of this study is to retrieve *T–t* information, using phosphate accessory phase textural relationships, compositional variation, and thermochronometers, for the Mesoproterozoic Honey Brook Upland (southeastern Pennsylvania, USA) and its Paleozoic sedimentary cover, the Chester Valley Sequence (CVS). As well as providing the first age estimates of Proterozoic and Paleozoic metamorphism affecting HBU and CVS, the derived *T–t* paths are discussed in the larger context of Grenvillian and Appalachian orogenesis.

2. Regional setting

The Piedmont of southeastern Pennsylvania was the subject of thorough investigative efforts in the early part of the 20th century, notably those of Florence Bascom of Bryn Mawr College, and her students Eleanora Bliss Knopf and Anna Jonas Stose (Bascom, 1905; Bascom et al., 1909; Bliss and Jonas, 1916; Stose and Jonas, 1922, 1923, 1927; Knopf and Jonas, 1923, 1929). Their contributions touching directly on the Honey Brook Upland and the Chester Valley Sequence include Bascom (1905) and Bascom and Stose (1932, 1938). Other early studies of the Upland centered on graphite-bearing rocks (Miller, 1912; Sandford and Lamb, 1949; Postel, 1951) and their potential economic significance. The nature of the Martic Line (or thrust), the contact between Cambro–Ordovician siliciclastic slope deposits and ocean basin pelites which forms the southern boundary of the Chester Valley Sequence (Fig. 1), was the subject of the classic paper by Cloos and Hietanen (1941).

The HBU is the subject of several student theses written between 1950 and 1990 (O'Neill, 1952; Waraska, 1952; Robelen, 1968; Dill, 1974; Huntsman, 1975; Demmon, 1977; Thomann, 1977; Organist, 1978; Pupa, 1988), and was sampled as part of a study on the Pb isotope systematics of Grenville-age crustal blocks in the eastern U.S. (Parks, 1993; Sinha et al., 1996). The field relations, petrography, and geochemistry of the Honey Brook anorthosite are addressed in Crawford et al. (1971). Valley and O'Neil (1981) and Crawford and Valley (1990) used carbon isotope partitioning on calcite–graphite mineral pairs to determine peak metamorphic temperatures in granulite- and amphibolite-facies samples from the HBU. The geologic history of the Honey Brook Upland and the Chester Valley Sequence is addressed in Crawford and Crawford (1980), Crawford and Hoersch (1984), and Crawford et al. (1999).

The Honey Brook Upland is a ~700 km^2 block of Proterozoic-age felsic to mafic gneiss, unconformably overlain by the CVS, a weakly metamorphosed, late Proterozoic to Ordovician quartz–carbonate–semipelite continental shelf-to-slope transition facies (Fig. 1). In gross lithological terms (Table 1), the Upland consists of two compositionally variable (felsic-to-mafic) subterranes. A low-pressure granuilite facies terrane in the northern part of the Upland is cored by the elliptical (~52 km^2) Honey Brook anorthosite (Crawford et al., 1971) (Fig. 1). The Brandywine Manor Fault forms most of the contact between the northern granulite terrane and an amphibolite-facies terrane in the southern portion of the Upland. Portions of felsic gneisses in both the granulite facies terrane and amphibolite facies terrane are graphite-bearing (Crawford and Hoersch, 1984; Crawford and Valley, 1990), and minor outcrops of diabase (late Proterozoic and Mesozoic), pegmatite, marble, serpentinite, and peridotite occur in both terranes (Bascom and Stose, 1938; Crawford and Crawford, 1980, Crawford and Hoersch, 1984; Sloto, 1994). Common mineral assemblages for the Honey Brook Upland rocks are given in Table 1; see also Crawford and Hoersch (1984).

Stratigraphy of the Chester Valley Sequence is treated in Stose and Jonas (1922, 1923), Bascom and Stose (1938), Meisler and Becher (1968), MacLachlan (1994), Faill (1997), and Kaufman (1999). In stratigraphic succession, the CVS consists of the Chickies Quartzite, the quartzitic and phyllitic Harpers and Antietam Formations, the carbonate bank sequence consisting of the dolomites and limestones (with admixed shales and sands) of the Vintage, Kinzers, Ledger, and Elbrook (~Zooks Corner) formations, and the slope-facies Conestoga Formation (see MacLachlan, 1994, for alternate stratigraphic assignments).

3. Methods

All images, element-distribution maps, quantitative and age-analyses presented in this paper were performed on the JEOL 733 Superprobe EMPA housed at Rensselaer Polytechnic Institute. Machine conditions for mapping and quantitative major- and trace-element analysis are given in Pyle and Spear (1999), Pyle et al. (2001) and Pyle (2001). Sample localities are presented in Table 2. Relevant major and accessory phase quantitative analyses are presented in Tables 3–7. Additional major-phase mineral analyses are available as electronic supplements at the URL listed below.

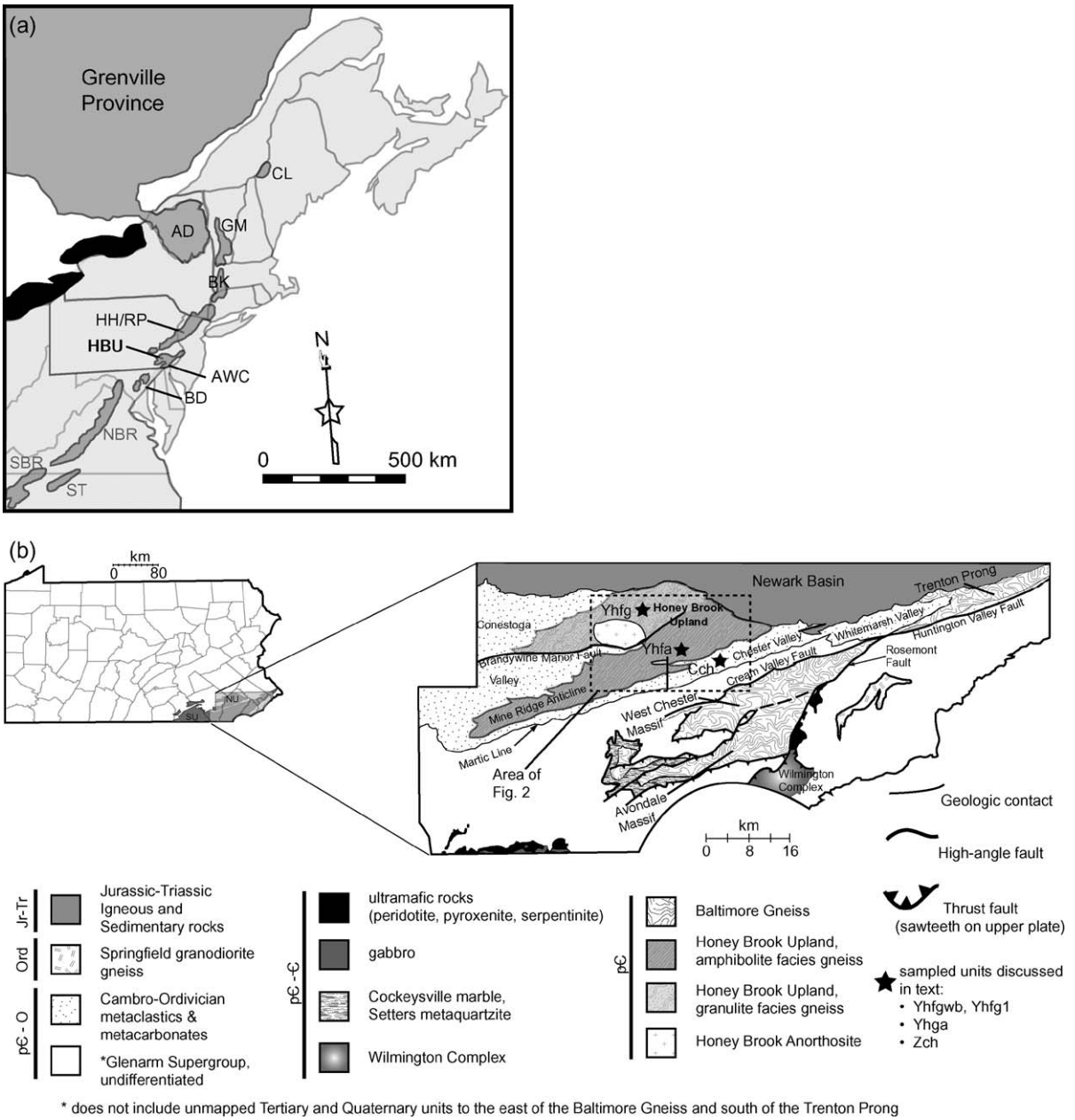

Fig. 1. (a) Simplified map of the NE United States and adjoining Canada showing the locations of the Grenville orogen, the Adirondacks (AD), and Appalachian Grenville inliers, including the Chain Lakes Massif (CL), Green Mountains (GM), Berkshire Massif (BK), Hudson Highlands and Reading Prong (HH/RP), Honey Brook Upland (HBU), Avondale/West Chester Massif (AWC), Baltimore Gneiss Domes (BD), Northern (NBR) and Southern (SBR) Blue Ridge, and Sauratown Mountain (ST). Modified after Rankin (1976). (b) Simplified geology of the Pennsylvania Piedmont upland. NU=northern Piedmont upland, SU=southern Piedmont upland. Map adapted from Crawford et al. (1999), using geology of Bascom et al. (1909), Berg et al. (1980), and Alcock and Wagner (1995).

Pyle et al. (2005) outline procedures followed for U–Th–total Pb EMPA dating of monazite. For each spot analysis, two independent ages are determined by simultaneous determination of Pb concentration on two wavelength dispersive spectrometers. In addition to techniques outlined in Pyle et al. (2005), age uncertainties are determined by Monte Carlo propagation (10,000 trials per age analysis) of U, Th, and both Pb compositional uncertainties through the U–Th–total Pb age equation of Montel et al. (1996). Monazite U–Th–total Pb spot analyses are given in Table 8. Spot "dates" are listed with ±1-sigma uncertainties, and weighted

Table 1
Map formation key for Fig. 2

Probable age	Symbol	Formation name	Description	Comments
Triassic	Tr	Triassic sediments	Undifferentiated Triassic clastic sediments	Newark Basin affinity
Jurrasic	JRd	Jurassic diabase	Fine-grained plagioclase-augite diabase	Newark Basin affinity
Ordovician–Cambrian	OCc	Conestoga Formation	Argillaceous limestone with thin phyllite layers	Chester Valley Sequence
Cambrian	Ce	Elbrook Formation	Laminated, fine-grained interbedded limestone and dolomite	Chester Valley Sequence
Cambrian	Cl	Ledger Formation	Medium-grained granular dolomite	Chester Valley Sequence
Cambrian	Ck	Kinzers Formation	Micaceous limestone with shaly interbeds	Chester Valley Sequence
Cambrian	Cv	Vintage Formation	Granular dolomite with basal knotted marble	Chester Valley Sequence
Cambrian–Proterozoic (Z)	CZah	Antietam/Harpers Formations, undiff.	Interbedded, laminated quartzite, quartzose schist and sandy micaceous schist	Chester Valley Sequence
Proterozoic (Z)	Zch	Chickies Quartzite	Vitreous quartzite with interbeds of quartzose schist and sandy micaceous schist, with basal conglomerate	Chester Valley Sequence
Precambrian–Ordovician	oct	Octoraro Phyllite	Quartz–muscovite–chlorite phyllite	South of Chester Valley
Precambrian–Ordovician	wb	Wissahickon schist	Quartzo-aluminous schist, generally amphibolite facies	South of Chester Valley
(Late) Proterozoic	um	Ultramafite	Pods and/or lenses of peridotite or pyroxenite, variably to completely altered to serpentinite	um S of Chester Valley distinct from um in HBU
Late Proterozoic	pg	Pegmatite	Coarse-grained dikes of Qtz + Alk Fsp ± Ms ± Bt	Honey Brook Upland
Late Proterozoic	md	Meta-diabase	Plagioclase-augite diabase altered to albite + epidote	Honey Brook Upland
Proterozoic (Y)	Ybfg	Granulite-facies felsic gneiss	Quartz + mesoperthite + plagioclase + orthopyroxene ± augite	South of Chester Valley
Proterozoic (Y)	Ybmg	Granulite-facies mafic gneiss	Hornblende + plagioclase + augite + orthopyroxene ± quartz ± garnet ± orthoclase ± biotite	South of Chester Valley
Proterozoic (Y)	Yhm	Marble	Coarsely crystalline graphitic marble, dolomitic in places	Honey Brook Upland
Proterozoic (Y)	Yhfa	Amphibolite-facies felsic gneiss	Quartz + alkali feldspar + plagioclase ± garnet ± biotite with secondary muscovite and epidote	Honey Brook Upland
Proterozoic (Y)	Yhma	Amphibolite-facies mafic gneiss	Hornblende + plagioclase ± quartz ± garnet ± biotite	Honey Brook Upland
Proterozoic (Y)	Yhia	Amphibolite-facies intermediate gneiss	Interlayered Yhfa and Yhma	Honey Brook Upland
Proterozoic (Y)	Yhga	Amphibolite-facies felsic gneiss, graphite-bearing	Graphite-bearing equivalent of Yhfa	Honey Brook Upland
Proterozoic (Y)	Yhfg	Granulite-facies felsic gneiss	Quartz + mesoperthite + plagioclase + orthopyroxene ± augite: more evolved varieties contain ferroaugite	Honey Brook Upland
Proterozoic (Y)	Yhmg	Granulite-facies mafic gneiss	Hornblende + plagioclase + augite + orthopyroxene ± quartz ± garnet ± orthoclase ± biotite	Honey Brook Upland
Proterozoic (Y)	Yhan	Anorthosite	Anorthosite plus gabbroic, leuco-gabbroic segregations	Honey Brook Upland

Table 2
Sample locality, rock type, and assemblage

Sample	Collection locality	Lithology	Major phase mineral assemblage	Accessory phase mineral assemblage	No. of thin sections analyzed
Yhfg1	PA SR 401 at Fairview Rd., E. Nantmeal Twp., 40.1225°N, 75.7146°W	Granulite-facies felsic gneiss (opdalite)	Qtz, Plg>Kfs, Opx>Cpx, Hbl, Bt (trace), Ilm	Zrn, Ap, Aln, Mnz (trace)	2 (yhfg1b, Yhfg1c)
Yhfgwb	Walnut Bank Rd., Wallace Twp., 40.0953°N, 75.7459°W	Granulite facies felsic gneiss (charnockite)	Qtz, Kfs>Plg, Cpx, Hbl, Bt (trace), Ti-Mt	Zrn, Ap, Aln	1 (Yhfgwb)
Yhga	Lower Pine Creek Rd, W. Pikeland Twp., 40.0830°N, 75.6129°W	Amphibolite-facies quartzofeldspathic gneiss	Qtz, Ksp>Plg, Grt, Ms (trace), Ilm, Rt (trace), Ttn (trace)	Zrn, Ap, Mnz, Aln (trace)	2 (Yhga1a, Yhga1b)
Zch	PA SR 282 at Shelmire Rd., E. Brandywine Twp., 40.0363°N, 75.7090°W	Quartzite	Qtz, Kfs (trace), Ms (trace)	Zrn, Mnz, Xno, Trm	1 (Zch1a)

Phase abbreviations after Kretz (1983). Where not included in Kretz, abbreviations Mnz (monazite) and Xno (xenotime) from Pyle et al. (2001).

average monazite domain ages are given in the text with ±2 standard errors of the mean.

4. Samples

Samples of anorthosite, mafic-to-felsic granulite-facies and amphibolite facies gneisses, and Cambro–Ordovician cover rocks were collected (circles, Fig. 2), sectioned, and examined for the presence or absence of monazite, xenotime, and apatite. Monazite+apatite±xenotime were identified in samples (Table 2) from three units (stars, Fig. 2): 1) granulite-facies felsic gneiss (Yhfg); 2) amphibolite-facies (±graphite) intermediate gneiss (Yhga); 3) metaquartzite (Zch).

4.1. Yhfg — granulite-facies felsic gneisses ("*opdalite*" and "*charnockite*")

Two compositional variants of granulite-facies felsic gneiss were examined. Sample Yhfg1 is an intermediate variety with a primary major-phase mineral assemblage of ~35 vol.% orthopyroxene ((Fe/(Fe+Mg) 0.58–0.60)+augite (0.48)+hornblende (0.61–0.69), ~15 vol.% quartz and ~50 vol.% mesoperthite ($Ab_{10}Or_{90}$ host, $Ab_{78}An_{22}$ perthite)+plagioclase ($Ab_{77}An_{22}Or_1$) in an approximate 4:1 plagioclase:K-feldspar volume ratio (an opdalite, after Streckeisen, 1976). Texturally primary accessory phases in this variant include zircon, allanite, ilmenite, and apatite.

Table 3
Representative compositions of apatite in opdalite (Yhfg1b, Yhfg1c) and amphibolite-facies felsic gneiss (Yhga1a)

Sample	Yhfg 1b	Yhfg 1b	Yhfg 1c	Yhfg 1c	Yhfa 1a	Yhfa 1a	Yhfa 1a	Yhfa 1a	Yhfa 1a	Yhfa 1a
Setting	Matrix	Matrix	Matrix	Matrix	Incl grt	Incl grt	Incl grt	Matrix	Matrix	Matrix
Number	1	2	4	6	1	8	9	6	7	11
CaO	55.73	56.45	56.74	56.68	56.55	56.80	56.81	56.44	55.41	55.92
P_2O_5	42.28	42.35	43.10	43.43	42.58	42.67	42.93	42.81	42.33	42.31
Cl	3.40	3.80	0.68	0.14	2.47	1.36	1.66	3.83	4.33	1.88
F	2.61	1.98	3.15	3.22	1.36	1.41	1.90	1.02	1.24	1.39
Total	104.02	104.58	103.67	103.47	102.96	102.24	103.30	104.10	103.31	101.50
–O=F	1.10	0.83	1.33	1.36	0.57	0.59	0.80	0.43	0.52	0.59
–O=Cl	0.77	0.86	0.15	0.03	0.56	0.31	0.37	0.86	0.98	0.42
New total	102.15	102.89	102.19	102.08	101.83	101.34	102.13	102.81	101.81	100.49
Ca	4.9695	5.0252	5.0156	5.0012	5.0833	5.1191	5.0678	5.0414	4.9925	5.0824
P	2.9789	2.9788	3.0103	3.0279	3.0243	3.0386	3.0260	3.0214	3.0136	3.0384
Total cations	7.9484	8.0040	8.0259	8.0291	8.1076	8.1577	8.0938	8.0628	8.0061	8.1208
Total anion minus OH	1.1666	1.0554	0.9170	0.8582	0.7121	0.5690	0.7346	0.8101	0.9469	0.6432
Clap	0.4111	0.5070	0.0951	0.0195	0.3512	0.1939	0.2342	0.5412	0.6171	0.2703
FAp	0.5889	0.4930	0.8219	0.8387	0.3609	0.3751	0.5003	0.2689	0.3298	0.3729
OHAp	n.d.	n.d.	0.0830	0.1418	0.2879	0.4310	0.2655	0.1899	0.0531	0.3568

Table 4
Representative analyses of monazite

Sample	Yhfg1b	Yhfg1b	Yhfg1b	Yhfg1c	Yhfg1c	Yhga1a	Yhga1a	Yhga1a	Yhga1a	Yhga1a	Yhga1a	Zch1a	Zch1a	Zch1a
Analysis	a-10	c-12	d-14	a-19	b-15	a-1	a-2	a-3	b-5	b-6	b-7	a-1	b-6	c-7
Location	In Hbl	In Ap	In Ap	Ap-Ilm gb	In Ap	Mtrx-c	Mtrx-c	Mtrx-ob	Mtrx-c	Mtrx-ob	Mtrx-r	mtrx	mtrx	In ksp
P_2O_5	29.81	31.09	30.10	29.25	30.25	25.54	27.35	27.59	27.40	28.05	28.86	28.92	29.16	30.01
SiO_2	0.97	0.10	0.12	0.10	0.29	2.70	1.26	1.42	1.60	1.22	0.48	1.24	0.59	0.24
CaO	0.26	0.82	1.39	0.55	1.24	1.70	1.65	1.55	1.60	1.51	1.37	0.16	0.08	0.12
PbO	0.13	0.02	0.04	0.02	0.00	0.75	0.58	0.56	0.67	0.64	0.40	0.05	0.09	0.00
ThO_2	1.99	0.05	0.25	0.04	0.10	19.03	12.61	12.62	13.57	10.88	7.61	2.13	2.34	0.78
UO_2	0.16	0.00	0.00	0.02	0.04	0.37	0.25	0.43	0.52	1.14	0.42	0.06	0.00	0.00
Y_2O_3	0.87	1.57	0.85	0.27	0.35	0.70	0.89	1.09	0.90	3.39	1.39	0.84	0.36	0.27
La_2O_3	18.71	15.56	14.39	23.20	23.84	7.38	7.72	8.42	9.12	9.93	9.01	16.21	16.42	19.33
Ce_2O_3	31.70	32.70	31.34	33.24	33.24	20.54	22.32	22.84	22.49	21.94	24.27	31.49	32.12	32.89
Pr_2O_3	2.99	3.55	3.80	2.59	2.57	2.85	3.16	2.95	2.93	2.58	3.26	3.15	3.27	3.11
Nd_2O_3	10.56	12.58	14.80	7.66	7.76	13.00	14.15	13.16	12.62	10.71	13.67	11.86	12.55	10.65
Sm_2O_3	1.17	1.61	2.06	0.59	0.57	2.78	3.36	3.15	2.81	2.47	3.62	1.71	1.39	1.07
Gd_2O_3	0.40	0.97	1.31	0.19	0.35	1.77	2.37	2.32	2.13	2.57	2.99	1.00	0.41	0.26
Tb_2O_3	0.00	0.19	0.19	0.00	0.08	0.13	0.17	0.19	0.13	0.28	0.27	0.15	0.04	0.00
Dy_2O_3	0.01	0.30	0.20	0.00	0.00	0.49	0.49	0.58	0.53	1.20	0.62	0.17	0.05	0.02
Er_2O_3	0.08	0.05	0.05	0.03	0.04	0.00	0.02	0.03	0.01	0.10	0.01	0.03	0.00	0.02
Total	99.81	101.18	100.90	97.74	100.72	99.73	98.35	98.90	99.03	98.61	98.26	99.14	98.86	98.77
Cat/4O	1.998	2.008	2.026	2.012	2.022	2.005	2.005	2.002	2.001	2.003	2.002	2.002	1.999	1.996
X_{LREE}	0.9554	0.9469	0.9569	0.9908	0.9851	0.7794	0.8432	0.8361	0.8300	0.7856	0.8810	0.9443	0.9642	0.9831
X_{HREE}	0.0064	0.0197	0.0227	0.0029	0.0062	0.0073	0.0074	0.0088	0.0078	0.0186	0.0090	0.0177	0.0066	0.0039
X_{Ac}	0.0196	0.0005	0.0023	0.0005	0.0013	0.1968	0.1285	0.1298	0.1410	0.1179	0.0783	0.0201	0.0215	0.0072
X_{YPO_4}	0.0185	0.0329	0.0180	0.0058	0.0074	0.0165	0.0209	0.0254	0.0212	0.0779	0.0318	0.0179	0.0077	0.0058

Values in wt.% oxide.

Table 5
Representative analyses of xenotime

Sample	Zch1a	Zch1a	Zch1a	Yhfg1b	Yhga1a
Analysis	a-3	a-4	b-5	a-13	a-4
Location	Mtrx-c	Mtrx-r	Og on Zrn	In Ap	In Ap
P_2O_5	32.12	31.56	31.08	32.15	33.98
SiO_2	0.18	0.25	0.31	0.23	0.73
CaO	0.00	0.01	0.00	5.86	0.32
PbO	0.02	0.08	0.05	0.00	0.01
ThO_2	0.23	0.18	0.32	0.08	0.12
UO_2	0.24	0.19	0.16	0.36	0.21
Y_2O_3	49.60	48.27	51.31	45.44	49.59
Nd_2O_3	0.22	0.16	0.41	0.21	0.34
Sm_2O_3	0.60	0.33	0.48	0.28	0.78
Eu_2O_3	0.23	0.12	0.03	0.01	0.03
Gd_2O_3	3.20	2.35	1.89	2.07	4.53
Tb_2O_3	0.57	0.72	0.47	0.59	0.84
Dy_2O_3	5.21	6.48	3.74	4.84	6.46
Ho_2O_3	1.01	1.20	0.75	1.00	0.82
Er_2O_3	3.72	4.01	3.09	3.47	1.61
Tm_2O_3	0.53	0.63	0.55	0.36	0.24
total	101.76	100.73	98.70	100.05	102.79
Cat/4O	2.046	2.047	2.052	2.123	2.033
X_{LREE}	0.0111	0.0066	0.0100	0.0061	0.0125
X_{HREE}	0.1783	0.1931	0.1424	0.1669	0.1665
X_{Ac}	0.0032	0.0026	0.0034	0.0034	0.0022
X_{YPO_4}	0.8074	0.7977	0.8443	0.8236	0.8188

Values in wt.% oxide.

Variant two (sample Yhfgwb) is a felsic gneiss with a primary major phase assemblage of ~5 vol.% Mn-bearing (1.5 wt.% MnO) ferroaugite (Fe/(Fe+Mg) 0.98)+~50 vol.% quartz and ~35 vol.% mesoperthite (Ab_5Or_{95} host, $Ab_{86}An_{13}Or_1$ perthite)+plagioclase ($Ab_{86}An_{13}Or_1$) in an approximate 1:4 Plg:Kfs ratio (charnockite, after Streckeisen, 1976). Texturally primary accessory phases in charnockite include pyrite, Ti-magnetite containing ilmenite lamellae, zircon, allanite, and apatite.

Quartz in both varieties of granulite-facies gneiss is extensively recrystallized, contains grain boundary sutures, and multiple (~5–20/mm^2) subdomains within single grains. Linear and undulose trains of fluid inclusions or fluid-filled healed fractures in quartz are ubiquitous.

Both varieties of granulite-facies gneiss contain secondary mineral parageneses (Fig. 3). In charnockite (Fig. 3a, b), alteration of Fe-augite includes both coronal overgrowths of quartz+blue-green Fe-hornblende and pseudomorphous replacement by quartz+magnetite+calcite, and a Fe–Ca (~3:1 atomic ratio) silicate with olivine (M_2Si_1) stoichiometry, but low oxide total (94–95 wt.%). In the opdalite, hornblende is rimmed by pale-green, low-Ti biotite, and orthopyroxene has a characteristic coronal structure (Fig. 3c, d)

Table 6
Reintegrated pyroxene sample compositions, sample Yhfg1b

Phase	Aug (host)	Pig (exsoln)	Cpx (re-int)	Opx (host)	Aug (exsoln)	"Pig" (re-int)
n	5	4	–	6	4	–
Area (%)	87.03	12.93		86.6	13.4	
SiO_2	50.88	49.42	50.69	49.96	50.70	50.06
Al_2O_3	1.69	0.62	1.55	0.56	0.52	0.56
TiO_2	0.24	0.08	0.22	0.14	0.02	0.12
FeO	15.59	35.25	18.13	35.06	30.73	34.48
MnO	0.35	0.79	0.40	0.69	0.65	0.68
MgO	9.45	11.87	9.77	12.88	12.33	12.81
CaO	20.82	1.34	18.30	0.74	4.68	1.26
Na_2O	0.62	0.02	0.54	0.01	0.14	0.03
K_2O	0.01	0.02	0.01	0.01	0.03	0.02
Total	99.65	99.41	99.78	100.05	99.81	100.02
Si	1.9569	1.9851	1.9605	1.9847	1.9994	1.9849
Al IV	0.0431	0.0149	0.0395	0.0153	0.0006	0.0151
Al VI	0.0337	0.0142	0.0313	0.0112	0.0235	0.0110
Ti	0.0069	0.0025	0.0063	0.0041	0.0006	0.0036
Fe 3+	0.0426	–	0.0370	–	–	0.0160
Fe 2+	0.4588	1.1842	0.5494	1.1646	1.0134	1.1326
Mn	0.0113	0.0268	0.0132	0.0231	0.0216	0.0228
Mg	0.5420	0.7110	0.5631	0.7628	0.7249	0.7570
Ca	0.8579	0.0578	0.7583	0.0314	0.1977	0.0537
Na	0.0464	0.0015	0.0408	0.0010	0.0110	0.0024
K	0.0004	0.0011	0.0005	0.0006	0.0017	0.0008
Total	4.0000	3.9992	4.0000	3.9988	3.9943	4.0000
FM	0.4584	0.6248	0.5830	0.6042	0.5830	0.5994
Wo norm	43.53	5.32	38.39	3.09	12.46	10.17
En norm	30.58	35.52	31.18	38.35	36.51	35.99
Fs norm	25.88	59.16	30.42	58.56	51.03	53.85
T °C at 1 atm			900			915
T °C at 0.5 GPa			918			943

Temps calculated using Lindsley and Andersen (1983) normalization scheme, 2-pyroxene thermometer. Sufficient Fe^{3+} assumed to back correct cations to 4.0.

consisting of (core to rim) enstatite: cummingtonite: quartz + calcite + biotite ± hornblende: biotite + hornblende. Orthopyroxene in some instances is replaced by quartz + calcite + magnetite.

4.2. Yhga — amphibolite facies quartzofeldspathic gneiss

Lithologies mapped as Yhfa, Yhia, and Yhga (Sloto, 1994, and references therein) are weakly to moderately foliated quartzofeldspathic gneisses containing less than 10 modal percent ferromagnesian minerals ± graphite. Crawford and Hoersch (1984) report biotite and garnet as the primary ferromagnesian minerals; the sample discussed here contains garnet (avg. $Py_{18}Alm_{75}Sps_3Grs_3$) but no biotite. K-feldspar (Ab_6Or_{94}) : Plagioclase($Ab_{83}An_{17}Or_1$) ratio is ~3 : 1, with approximately 20 mol% quartz. Brittle-deformation features and fluid-inclusions are characteristic of quartz from this sample, and are virtually identical to analogous features developed in quartz in the granulite-facies gneisses.

Alkali feldspar and quartz are generally unaltered, but plagioclase is extensively replaced by epidote + muscovite + secondary albite (Fig. 3e). Garnet is subhedral to anhedral, pervasively fractured, and is extensively rimmed by chlorite and replaced by fine-grained intergrowths of muscovite + epidote. Discrete reaction zones around garnet (Fig. 3f) are defined by fine-grained epidote, perthite-free alkali feldspar, and either discrete muscovite or symplectitic intergrowths of muscovite + quartz. Reaction zones between K-feldspar and garnet contain muscovite–biotite–quartz–epidote intergrowths. Ilmenite is the primary Fe–Ti oxide, but is extensively rimmed by rutile + titanite.

4.3. Zch — Chickies Quartzite (greenschist-facies metaquartzite)

Zch is a massive, moderately foliated orthoquartzite with flattened quartz and feldspar pebbles. Flattened quartz pebbles contain subdomains and display undulose extinction, but matrix quartz grains possess equi-

Table 7
Compositions used in accessory phase geothermometry

Part I. Garnet (YAG)–xenotime and garnet (YAG)–monazite thermometry, sample Yhga1

Set	X_{Grs}	X_{YAG}	X_{An}	X_{OHAp}	X_{YPO4}, Mnz	P (GPa)	f_{H2O}[a] (GPa)	T Grt(YAG)-Mnz range	T YAG-Xno
1	0.027(c)–0.040(r)	0.0017(c)	0.17	0.30–0.25 (incl in Grt)	0.0399 (LL core)	0.5	0.17–0.34	489–511 °C	523 ± 14 °C
2	0.027(c)–0.040(r)	0.0013(r)	0.17	0.20–0.08 (matrix)	0.0525 (median core)	0.5	0.17–0.34	512–544 °C	535 ± 16 °C
3	0.04 (r)	0.0013(r)	0.17	0.08	0.0779 (UL core)	0.5	0.17–0.34	555–560 °C	535 ± 16 °C
4	0.027(c)–0.040(r)	0.0017(c)	0.17	0.30–0.25 (incl in Grt)	0.0152 (LL rim)	0.5	0.17–0.34	458–479 °C	–
5	0.027(c)–0.040(r)	0.0013(r)	0.17	0.20–0.08 (matrix)	0.0253 (UL rim)	0.5	0.17–0.34	487–518 °C	–

Part II. Monazite–xenotime thermometry[b]

Set	Textural setting	$X_{(Y+HREE)PO_4}$, Mnz	$X_{(Y+HREE)PO_4}$, Xno	T P et al.[c]	T G and H[d]	T_{Th} S–G et al.[e]
Sample Yhga1						
1	Matrix monazite, core domain	0.0508–0.0965	0.9880	424–616 °C	417–699 °C	440–703 °C
2	Monazite + xenotime inclusions in apatite	0.1083–0.1299	0.9880	650–705 °C	749–829 °C	751–825 °C
Sample Yhfg1b						
1	Monazite + xenotime inclusions in apatite	0.0408–0.0526	0.9905	358–434 °C	320–432 °C	349–454 °C
Sample Zch1a						
1	Matrix monazite + xenotime	0.0508	0.9857	318 °C	261 °C	294 °C

[a] Fugacity range calculated at $500 \leq T \leq 650$ °C, $0.75 \leq X_{H_2O} < 1.00$.
[b] 2σ on T estimates ± 50 °C; where required (Gratz and Heinrich calibration), P fixed at 0.5 GPa.
[c] Empirical calibration (logarithmic fit) of Pyle et al. (2001).
[d] Experimental calibration of Gratz and Heinrich (1997).
[e] Experimental calibration of Seydoux-Guillaume et al. (2002), corrected to $X_{Th,Mnz} = 0.09$.

librium (triple-junction) grain boundaries with little to no grain boundary suturing. Muscovite + tourmaline-rich layers are present, but these two phases also occur dispersed in minor amounts throughout the matrix. Zircon, monazite, and xenotime are present in the matrix; apatite was not identified. Barite occurs solely as inclusions within K-feldspar.

5. Petrography of accessory phosphates

5.1. Granulite-facies felsic gneisses (opdalite (Yhfg1), charnockite (Yhfgwb))

Apatite is an abundant (0.5–3 vol.%), texturally primary accessory phase in charnockite and opdalite. Apatite size ranges from 100s to 1000s of μm (Fig. 4a,b). Primary apatite is commonly rimmed by secondary allanite (Fig. 4c), and also has textural relationships with secondary monazite that indicate recrystallization and compositional alteration of primary apatite have occurred (see below).

No monazite was observed in Yhfgwb, but monazite is a common secondary accessory phase in Yhfg1, along with subordinate xenotime. Secondary monazite is found as fracture fill in primary allanite (Fig. 4d), as non-oriented grain-boundary decorations on apatite (Fig. 4e), as inclusions in zircon rims (Fig. 4f), and is included in biotite + hornblende coronas around orthopyroxene (Fig. 4g). Monazite and xenotime also occur as fine, acicular inclusions (Fig. 4h, i), oriented parallel to the c axis of apatite, a widely documented texture in high-grade apatite-bearing rocks (Amli, 1975; Harlov et al., 2002; Hecht and Cuney, 2000; Harlov and Forster, 2003).

5.2. Yhga1 — amphibolite-facies quartozfeldspathic gneiss

Subhedral to anhedral apatite occurs included in garnet, within poly-phase inclusions in garnet (Fig. 5a, b), and as a matrix phase (Fig. 5c). Apatite is 50–200 μm in short dimension, with typical aspect ratios between 2 : 1 and 3 : 1. Texturally primary apatite commonly contains grain boundary or fracture decorations of monazite, xenotime, or allanite (see below).

Monazite is generally present as a matrix phase. Primary monazite (Fig. 5d–f) generally consists of dark (in terms of back-scatter electron intensity contrast (BEIC)) cores surrounded by brighter BEIC overgrowths. The majority of the grain may consist of overgrowth (Fig. 5d), or the overgrowth may form very thin rims (Fig. 5e). Where the majority of the grain is a "dark core", zoning in this core may be patchy or mottled (Fig. 5e). Additionally, monazite crossed by or adjacent to fractures (Fig. 5f) forms dark rims and domains gener-

Table 8
U–Th–total Pb EMPA age analyses of monazite from Honey Brook Upland/Chester Valley, SE Pennsylvania, USA

Part I. Calibration and correction information

Date	el	# cal	C/nA•s	s	nA (cup)	1–σ (%)	CF Pb interference	CF U interference
9/03	Y	4	493.7	20	10.02	0.36	0.003656 ± 0.000095 Pb4 (5), 0.003481 ± 0.000026 Pb5 (5)	–
9/03	Ce	4	259.7	20	10.03	0.47	–	–
9/03	Th	4	83.6	20	10.04	0.79	–	–
9/03	U	4	188.1	20	10.03	0.53	0.001565 ± 0.000080 Pb4 (5), 0.001540 ± 0.000098 Pb5 (5)	0.002617 ± 0.000067 (5)
9/03	Pb4	5	63.9	20	10.03	0.89	–	–
9/03	Pb5	5	55.2	20	10.03	0.95	–	–
11/03	Y	4	486.3	20	10.02	0.37	0.003396 ± 0.000133 Pb4 (5), 0.003311 ± 0.000051 Pb5 (5)	–
11/03	Ce	4	265.6	20	10.03	0.46	–	–
11/03	Th	4	85.9	20	10.04	0.78	–	–
11/03	U	4	191.3	20	10.03	0.53	0.001635 ± 0.000103 Pb4 (5), 0.001585 ± 0.000068 Pb5 (5)	0.001990 ± 0.000069 (5)
11/03	Pb4	5	63.8	20	10.03	0.89	–	–
11/03	Pb5	5	56.4	20	10.03	0.95	–	–
9/04	Si	1	155.09	20	10.02	1.00		
9/04	Ca	1	244.2	20	10.04	0.48		
9/04	Y	1	303.3	20	10.06	0.45	0.004381 ± 0.000126 Pb4 (3), 0.004255 ± 0.000084 Pb5 (3)	–
9/04	Ce	1	100.1	20	9.99	0.74	–	–
9/04	Th	1	48.1	20	10.02	1.04	–	–
9/04	U	3	103.2	20	9.96	0.72	0.002213 ± 0.000101 Pb4 (3), 0.002014 ± 0.000075 Pb5 (3)	0.007021 ± 0.000182 (3)
9/04	Pb4	1	40.9	20	10.02	1.12	–	–
9/04	Pb5	1	37.2	20	10.02	1.17	–	–

Part II. Analysis information

Grain/spot/cycle	Th	Y	U*	Pb4*	Pb5*	1σ U (%)	1σ Th (%)	1σ Pb4 (%)	1σ Pb5 (%)	Age 4 (Ma)	1σ (m.y.)	Age 5 (Ma)	1σ (m.y.)	Spot avg age (Ma)	Expected spot 1σ (m.y.)	Expected spot s.e. (m.y.)
Sample Yhfg1b, granulite-facies intermediate gneiss (mangerite), Honey Brook Upland																
1/1/1	1.49	2279	1122	499	467	8.32	1.28	13.45	14.55	596	80	557	81	577	80	57
1/2/1	1.49	2508	1075	494	570	8.65	1.28	13.51	12.09	595	78	684	80	639	79	56
2/1/1	10.10	1924	2512	3563	3501	3.21	0.93	2.18	2.27	721	17	709	17	715	17	12
Sample Yhga1a, amphibolite-facies felsic gneiss, Honey Brook Upland																
1/1/1	13.85	2811	2670	6499	6657	3.47	0.92	1.58	1.65	969	17	992	18	981	18	12
1/1/2	13.80	2740	2839	6489	6556	3.29	0.94	1.58	1.66	967	17	977	18	972	17	12
1/2/1	10.77	3929	1754	4927	4920	5.02	0.94	1.85	1.96	954	19	953	20	954	20	14
1/2/2	10.72	3789	1681	4728	4809	5.18	0.94	1.91	2.00	923	19	938	20	931	20	14
1/4/1	12.19	4548	2073	5523	5592	4.33	0.94	1.73	1.82	943	18	955	19	949	19	13
1/4/2	12.18	2798	2100	5623	5689	4.27	0.94	1.71	1.80	960	18	971	19	966	18	13
1/5/1	10.71	3486	1765	4707	4920	4.98	0.94	1.92	1.97	917	19	958	21	938	20	14
1/5/2	10.75	3686	1801	4809	5005	4.91	0.94	1.89	1.95	933	19	970	21	951	20	14
1/6/1	11.99	3747	2100	5459	5497	4.27	0.94	1.74	1.83	946	18	953	19	950	19	13
1/6/2	12.00	3792	1978	5385	5395	4.49	0.94	1.76	1.86	936	18	938	19	937	19	13
2/1/1	10.49	4332	1600	4858	4874	5.39	0.94	1.87	1.97	969	20	972	21	971	20	14
2/1/2	10.44	4483	1720	4946	4882	5.08	0.94	1.85	1.98	987	20	974	21	981	20	14
2/2/1	11.56	4263	3432	5534	5708	2.88	0.94	1.74	1.80	958	18	987	20	972	19	13
2/2/2	11.64	4342	3447	5590	5925	2.86	0.94	1.72	1.76	961	18	1016	19	989	19	13
2/3/1	10.84	19,510	8106	6441	6462	1.45	0.94	1.59	1.69	1040	18	1043	19	1042	18	13
2/3/2	10.85	19,601	7917	6228	6572	1.49	0.94	1.63	1.68	1011	18	1064	19	1038	18	13
2/4/1	7.31	7435	3022	3683	3954	3.30	0.94	2.28	2.28	972	23	1041	25	1007	24	17
2/4/2	7.43	7381	2947	3692	3991	3.38	0.94	2.28	2.28	964	23	1039	25	1002	24	17
2/5/1	10.29	10,397	4457	5274	5345	2.33	0.94	1.78	1.89	983	19	996	20	989	19	14
2/5/2	10.26	9420	4311	5333	5427	2.40	0.94	1.78	1.86	1000	19	1017	20	1009	20	14
2/6/1	10.00	6003	3149	5023	5063	3.11	0.94	1.85	1.96	998	20	1005	21	1002	21	15
2/6/2	10.01	6018	3025	4866	5096	3.24	0.94	1.90	1.93	970	20	1015	21	993	21	14
3/1/1	8.48	13,909	7311	5095	5290	1.59	0.94	1.83	1.90	1021	20	1058	21	1039	20	14
3/1/2	8.40	13,759	7602	5062	5200	1.53	0.94	1.84	1.92	1013	19	1039	21	1026	20	14
3/2/1	11.92	15,783	7746	6740	7035	1.50	0.95	1.57	1.62	1018	17	1060	18	1039	18	13

(continued on next page)

Table 8 (*continued*)

Part II. Analysis information

Grain/spot/cycle	Th	Y	U*	Pb4*	Pb5*	1σ U (%)	1σ Th (%)	1σ Pb4 (%)	1σ Pb5 (%)	Age 4 (Ma)	1σ (m.y.)	Age 5 (Ma)	1σ (m.y.)	Spot avg age (Ma)	Expected spot 1σ (m.y.)	Expected spot s.e. (m.y.)
Sample Yhga1a, amphibolite-facies felsic gneiss, Honey Brook Upland																
3/2/2	11.99	15,649	7677	6769	6998	1.51	0.94	1.56	1.64	1019	17	1052	19	1035	18	13
3/3/1	11.27	4262	3798	5683	5859	2.66	0.94	1.72	1.80	995	19	1025	20	1010	19	14
3/3/2	11.45	4270	3861	5662	5654	2.61	0.94	1.71	1.84	976	18	975	32	976	19	13
3/4/1	8.96	19,073	7734	5345	5542	1.51	0.94	1.78	1.85	1014	19	1049	27	1031	20	14
3/4/2	9.02	18,939	7634	5335	5405	1.53	0.94	1.79	1.88	1010	19	1022	27	1016	20	14
4/1/1	14.94	4522	626	6150	6274	9.45	0.94	1.64	1.73	895	86	913	88	904	17	12
4/1/2	14.76	4492	778	6079	6175	8.32	0.94	1.66	1.74	892	76	906	77	899	21	15
4/2/1	7.42	15,347	5356	3732	3890	2.03	0.93	2.26	2.33	892	28	929	30	910	22	15
4/2/2	7.35	15,425	5536	3715	3864	1.99	0.94	2.27	2.34	889	28	923	30	906	21	15
4/3/1	7.89	12,887	7021	4734	4731	1.63	0.94	1.94	2.05	1012	27	1012	28	1012	21	15
4/3/2	7.87	12,756	7223	4735	4834	1.59	0.94	1.93	2.03	1008	27	1028	28	1018	16	11
4/4/1	15.94	4621	2307	6360	6431	3.80	0.94	1.61	1.70	840	36	849	36	845	15	11
4/4/2	16.18	4241	2160	6268	6497	4.01	0.94	1.62	1.69	819	36	848	38	834	22	15
5/1/1	8.41	14,299	3128	4101	4134	3.17	0.93	2.12	2.24	954	37	961	38	957	22	15
5/1/2	8.40	14,071	3335	4111	4210	2.99	0.94	2.13	2.20	950	36	972	37	961	21	15
5/2/1	7.39	13,927	7453	4231	4382	1.56	0.94	2.09	2.16	940	26	972	27	956	21	15
5/2/2	7.34	13,904	7484	4290	4357	1.56	0.94	2.08	2.17	956	26	971	27	963	33	23
5/3/1	3.30	8353	5719	2537	2671	1.94	0.99	3.06	3.11	1060	40	1113	42	1086	33	23
5/3/2	3.32	8300	5819	2573	2535	1.92	0.98	3.02	3.27	1064	39	1049	41	1057	19	13
6/1/1	9.88	17,520	7566	5551	5750	1.56	0.95	1.74	1.83	981	25	1015	26	998	19	13
6/1/2	9.71	17,503	7270	5534	5630	1.61	0.94	1.75	1.86	999	26	1016	27	1007	20	14
6/2/1	10.01	11,682	5435	5464	5566	1.98	0.94	1.77	1.86	1013	29	1031	30	1022	19	14
6/2/2	10.21	11,370	5299	5571	5478	2.03	0.94	1.75	1.88	1019	29	1003	29	1011	20	14
6/4/1	10.46	7327	4309	5405	5329	2.38	0.94	1.79	1.92	997	31	983	31	990	20	14
6/4/2	10.42	7579	4265	5371	5345	2.41	0.94	1.79	1.92	995	31	991	32	993	19	13
6/5/1	11.87	8415	3889	5930	6149	2.60	0.94	1.69	1.75	989	32	1024	34	1006	19	13
6/5/2	11.85	8713	3913	6035	6185	2.59	0.95	1.66	1.74	1007	32	1031	34	1019	17	12
Sample Yhga1b, amphibolite-facies felsic gneiss, Honey Brook Upland																
1/1/1	8.13	17,404	8690	5074	5359	1.89	1.17	2.09	2.08	1006	22	1060	23	1033	23	16
1/2/1	9.67	15,434	8454	5847	6057	1.91	1.16	1.92	1.96	1024	21	1059	22	1041	22	15
1/3/1	13.33	9413	9001	7453	7497	1.80	1.16	1.71	1.77	1000	19	1006	20	1003	19	14
1/4/1	9.94	20,841	9496	5973	6284	1.77	1.16	1.91	1.92	997	21	1047	21	1022	21	15
1/5/1	14.29	9168	6902	7428	7417	2.13	1.16	1.71	1.78	982	19	981	19	982	19	14
12/1/1	12.30	13,201	6005	6440	6591	2.41	1.16	1.83	1.89	988	20	1010	21	999	20	14
12/2/1	10.87	14,931	5613	5760	5733	2.57	1.16	1.95	2.03	992	22	987	22	989	22	15
12/4/1	14.50	6893	4791	6908	7023	2.75	1.16	1.79	1.83	944	19	959	20	951	20	14
12/5/1	16.59	6304	2838	7756	7924	3.74	1.16	1.68	1.74	972	19	993	20	983	20	14
Sample Zch1a, greenschist-facies metaquartzite (Chickies Formation), northern Chester Valley																
1/1/1	1.75	4191	2208	221	170	39.22	1.58	26.70	33.78	272	73	209	68	240	71	50
1/2/1	1.15	1994	1776	87	131	52.59	1.95	59.60	46.81	163	84	244	107	204	96	68
A/1/1	1.74	4043	1901	231	245	42.87	1.57	26.64	26.18	286	75	303	77	295	76	54
B/1/1	5.66	5315	3905	926	1034	16.99	1.16	7.55	7.17	358	27	399	31	378	29	21
B/2/1	4.79	3815	1226	801	851	27.68	1.19	8.86	8.63	370	33	394	35	382	34	24
C/1/1	1.32	1921	6717	132	200	18.64	1.81	44.37	33.62	193	85	291	101	242	93	66
D/2/1	3.24	2839	1163	442	459	37.17	1.28	14.98	14.92	302	45	313	47	307	46	33
E/1/1	1.78	2868	9600	307	471	13.28	1.56	21.81	15.63	329	49	501	74	415	62	50

2003 analyses performed at 25 kV; 2004 analyses performed at 15 kV.

ally, but not always, external to the bright BEIC domains. No monazite inclusions were identified in garnet, though a single monazite inclusion in K-feldspar was observed. No preferred orientation of monazite was noted.

Phosphate phases in the amphibolite-facies gneisses form a number of secondary accessory phase parageneses, which include both REE silicate (allanite) and REE phosphate. Monazite rims (Fig. 5g), and less

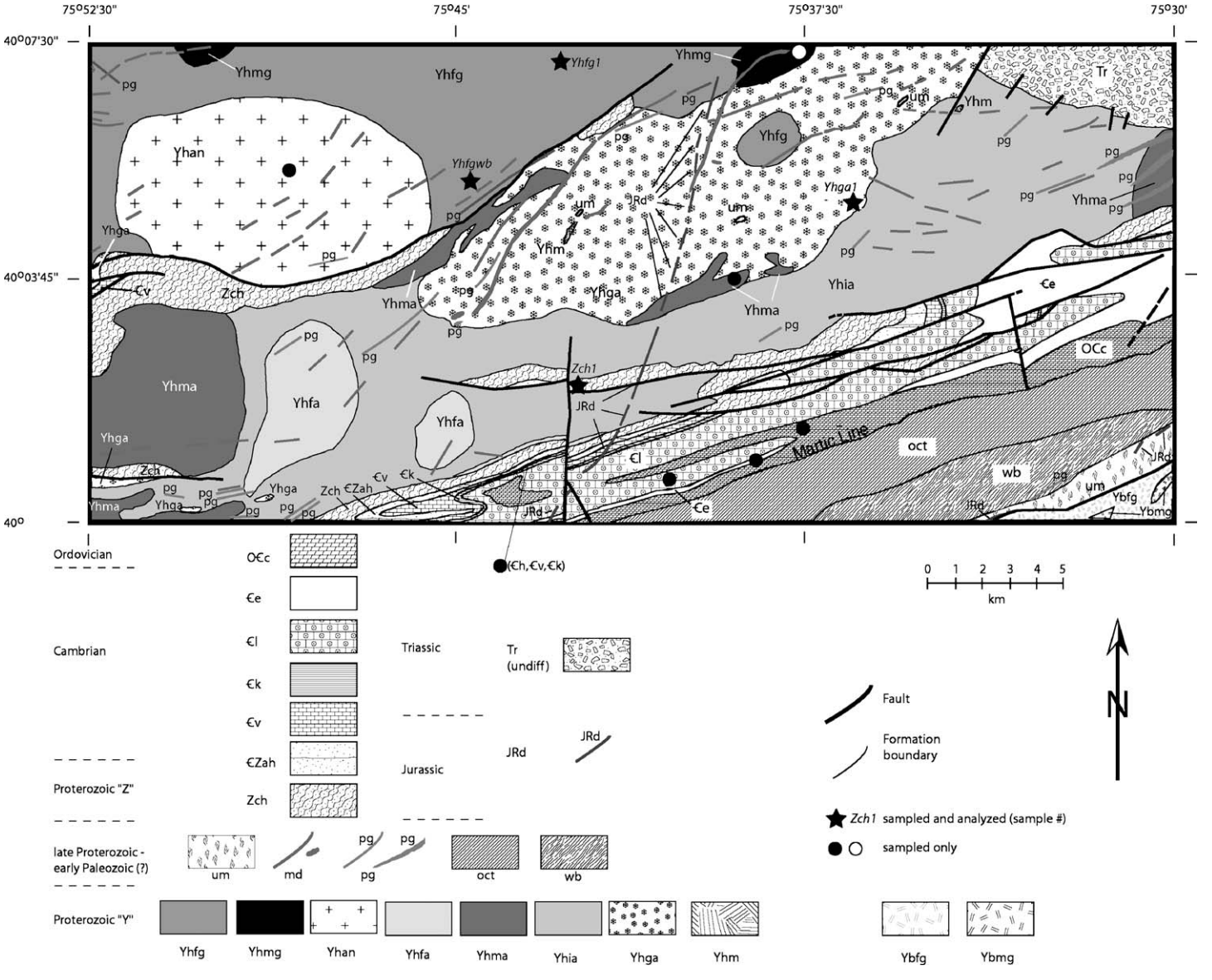

Fig. 2. Detailed geologic map of field area showing sample locations. Geology, structures, and unit designations are after Sloto (1994). Sample locales indicated by circles; locations of samples analyzed by EMPA for this study indicated by stars.

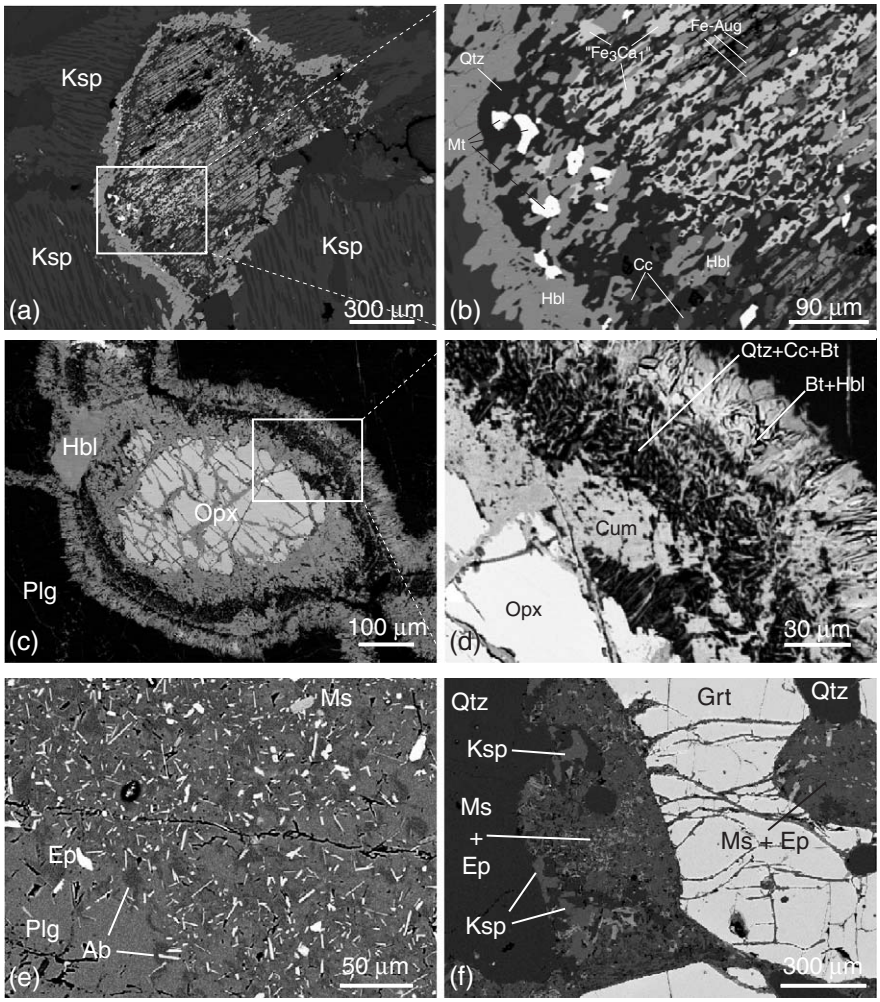

Fig. 3. (a, b) Back-scatter electron intensity (BEI) contrast image of replacement of ferroaugite (sample Yhfgwb) by Qtz, Mt, Cc, Hbl, and "Fe_3Ca_1", a Ca-bearing Fe-rich phase with Fe and Ca present in the indicated atomic ratio. Expanded area shown in (b) indicated on (a) with box. (e, f) BEI image of altered ferroaugite showing detail of exsolution structure, with "Fe_3Ca_1", Opx, and Pig lamellae present. (c, d) BEI contrast image of coronal structure developed on primary igneous orthopyroxene, sample Yhfg1b. Enlarged image in (d) shows coronal succession Opx: Cum: Qtz+Cc+Bt: Bt+Hbl. (e) Replacement of primary plagioclase by epidote+muscovite+albite, sample Yhga1a. (f) Detail of garnet+non-perthitic K-feldspar replacement by epidote+muscovite, sample Yhga1a. Scale indicated at base of each panel.

commonly, apatite rims (Fig. 5h) are surrounded by secondary, non-oriented sprays of allanite. Oriented inclusions and grain boundary decorations of monazite and xenotime are developed in and around apatite (Fig. 5i), similar to the texture observed in Yhfg1. Where this texture is observed in the amphibolite facies gneisses, secondary allanite may be present as a grain boundary decoration, but is not included in apatite.

5.3. Zch — metaquartzite

Monazite is fine-grained (≤15 µm), and occurs in the sample matrix (Fig. 6a) and as inclusions in flattened K-feldspar pebbles (Fig. 6b). No preferred orientation is noted in either case. Monazite in Zch is much less strongly zoned than monazite in Yhga (Figs. 6a, b and 5d–f).

Xenotime occurs in Zch as discrete matrix grains (Fig. 6c), and as epitaxial overgrowths on zircon (Fig. 6d). Xenotime is less abundant than monazite, and the observed matrix grains display greater BEIC (Fig. 6d) than monazite in this sample (e.g., Fig. 6b).

6. Accessory phase mineral chemistry

6.1. Apatite

Representative analyses of apatite in opdalite (Yhfg1b, Yhfg1c) and quartzofeldspathic gneiss (Yhga1a) are

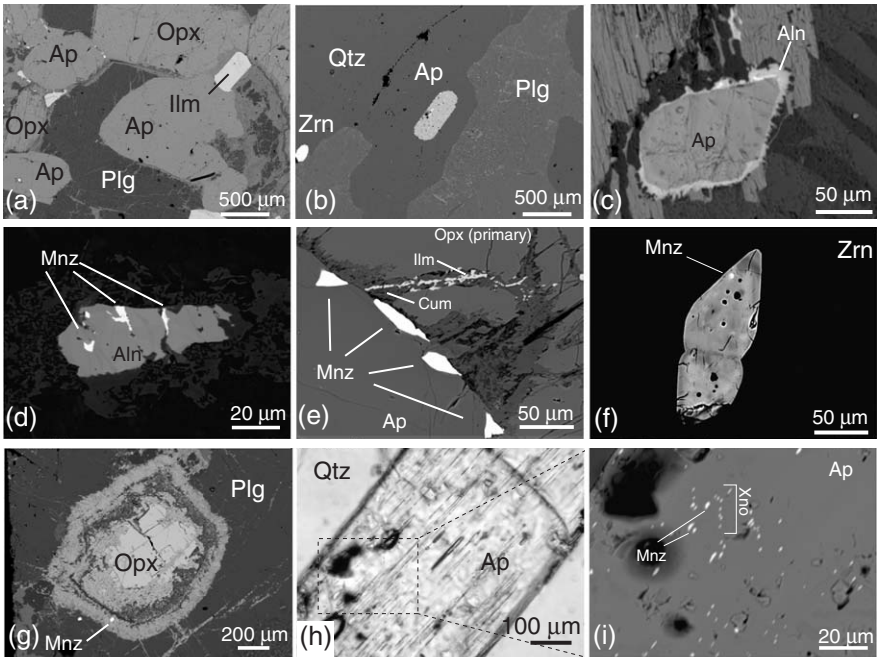

Fig. 4. BEI contrast images of primary and secondary phosphate accessory minerals in opdalite (Yhfg1b, Yhfg1c) and charnockite (Yhfgwb). (a) Millimetric, subequant, inclusion-free apatite plus subordinate ilmenite, sample Yhfg1c. (b) Elongate, inclusion-rich apatite, sample Yhfg1b. (c) Small (~100 µm), subequant, primary apatite rimmed by secondary allanite, sample Yhfgwb. (d) Secondary fracture infill of monazite in primary allanite, sample Yhfg1b. (e) Secondary monazite grain-boundary decorations on primary apatite, sample Yhfg1c. (f) Di-pyrimidal habit zircon with inclusion of Th-rich monazite, sample Yhfg1b. (g) Secondary monazite developed within fracture zone in Bt+Hbl corona around Opx, sample Yhfg1b. (h, i) photomicrograph (h) and BEI contrast image (i) of oriented inclusions of monazite and xenotime in primary apatite. Scale indicated at base of each panel.

listed in Table 3, and all analyses are plotted in Fig. 7a. All apatite analyses are regressed to time-zero F and Cl concentrations (Fig. 7b) in order to correct for beam-induced outward diffusion of F and Cl during apatite analysis (Stormer et al., 1993).

Two compositional populations of apatite are present in opdalite. Small (≤250 µm length) apatite containing a moderate to high density of monazite ± xenotime inclusions (e.g., Fig. 4h, i) are essentially FAp–OHAp solid solutions (open circles, Fig. 7a), and large (≥750 µm length) apatite with a low density of monazite ± xenotime inclusions (e.g. Fig. 4a) are ~50:50 FAp–ClAp solid solutions with zero calculated OHAp component (solid black circles, Fig. 7a.

Apatite in sample Yhga also displays systematic compositional trends. Apatite inclusions in garnet (open black squares, Fig. 7a) and matrix apatite (solid black squares, Fig. 7a) overlap in both FAp and OHAp content, but matrix apatite contains a higher maximum ClAp component (0.62) than does apatite included in garnet (0.38). A matrix apatite with abundant monazite and xenotime grain boundary decorations (Fig. 5i; solid gray square, Fig. 7a) is depleted in ClAp component relative to 3 of the 5 other matrix apatite analyses. Maximum calculated OHAp component in Yhga (0.43) is higher than the maximum calculated OHAp component (0.22) in the opdalite (Yhfg1).

The spatial association of secondary monazite inclusions in primary Cl-bearing apatite with a second generation of Cl-poor F-apatite is shown for sample Yhfg1c (Fig. 7c). Where large, texturally primary apatite (Ap 1, Fig. 7c) is free from monazite inclusions, it contains 10–30 mol% more Cl-component than recrystallized domains of secondary, F-dominant apatite (Ap 2) within the primary apatite and surrounding or abutting monazite inclusions (Fig. 7c). Although the texture of the *overall* apatite grain is primary, there has been small-scale (≤30 µm) internal compositional and crystallographic modification of the original homogeneous apatite. Where monazite inclusions are absent, the apatite composition is unmodified.

6.2. Monazite and xenotime chemistry

No monazite is observed in sample Yhfgwb; representative analyses of monazite from Yhfg1, Yhga1, and Zch are given in Table 4, and quantitative monazite analyses are plotted in Fig. 8.

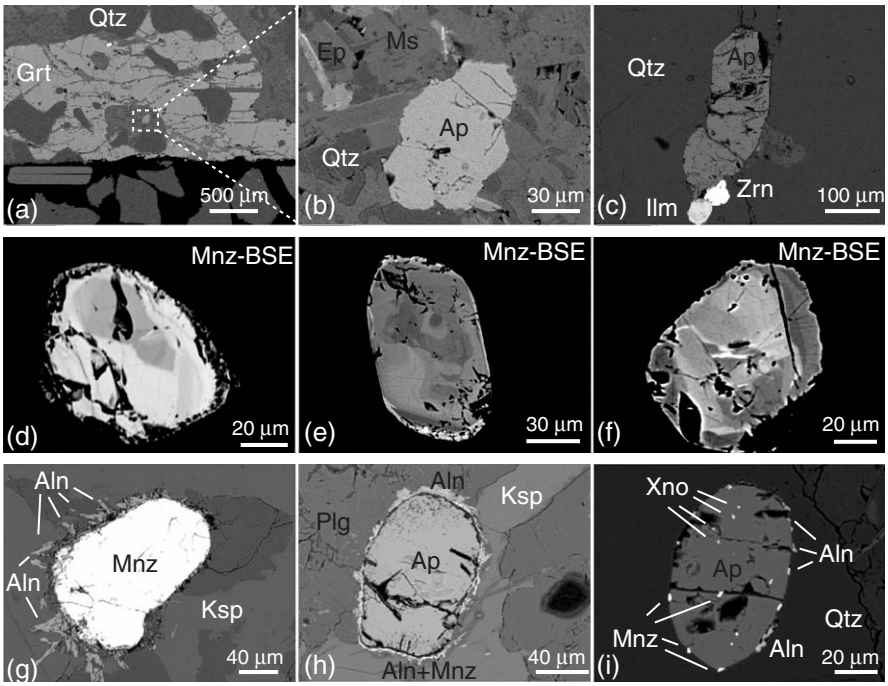

Fig. 5. BEI contrast images of primary and secondary phosphate accessory minerals in garnet-bearing, amphibolite-facies felsic gneiss (sample Yhga1). (a, b) Apatite within poly-phase inclusion (Ms+Ep+Qtz) in garnet. (c) Matrix apatite associated with ilmenite and zircon. (d–f) Subhedral, sub-equant monazite grains, displaying characteristic dark (high-Y) cores (d,e), bright (high-Th) overgrowths (d–f), and dark, low-Y, low-Th rims (f) adjacent to fractures. (g) Primary monazite rimmed by sprays of randomly oriented allanite. (h) Primary apatite rimmed by allanite with small intergrowths of secondary monazite. (i) Primary matrix apatite with inclusions of monazite plus xenotime and grain-boundary decorations of monazite plus allanite. Scale indicated at base of each panel.

Significantly higher (Y+HREE) and actinide (e.g., Th+U) components distinguish monazite in sample Yhga1 from monazite in Yhfg1 and Zch (Fig. 8a). For sample Yhga1, actinide content ranges from 8 to 20 mol%, with Y+HREE component between 2 and 10 mol%. Monazite from Yhfg1 to Zch is compositionally similar; monazite in Zch is slightly more enriched in actinide component, and monazite (Y+HREE) component is similar in monazite from both samples.

Monazite substitution trends (e.g., Förster, 1998) are shown in Fig. 8b and c; the brabantite exchange ($Ca(Th,U)REE_{-2}$) plots as a vector with an origin at (8,0) and a slope of −0.5; the huttonite exchange vector ($(Th,U)SiREE_{-1}P_{-1}$) has the same origin, but a slope of −1.0. Regression lines to data from each sample have slopes of −0.96 (Yhga1, $R^2=0.99$), −1.15 (Zch, $R^2=0.96$), and −1.01 (Yhfg1, $R^2=0.83$). In sample Yhga (circles), the exchange is a true (e.g. ThSi) huttonite component; (Th+U) in excess of Ca is virtually balanced by Si (Fig. 8d). Monazite in Zch (metaquartzite) generally falls along the huttonite exchange trend (circles, Fig. 8d), but the overall Th content of monazite in Zch is much lower than that of monazite in Yhga (Fig. 8a, b).

In contrast, secondary monazite inclusions in apatite, sample Yhfg1 (triangles) are distinguished by excess Si over Th+U–Ca and excess Ca over Th+U (Fig. 8d). This observation is consistent with the formation of monazite from the lessingite component of apatite, e.g., $Ca_4Ce(PO_4)_2(SiO_4)F$. Monazite in the Bt+Hbl corona around Opx (Fig. 4g; arrowed data in Fig. 8c, d) is compositionally distinct from the apatite-hosted monazite in the same sample.

Monazite element distribution maps (Fig. 9) show that much of the variation in back-scatter electron intensity contrast (Fig. 5) is due to inversely correlated variations in Th (Fig. 9b) and Y (Fig. 9d) content. In such cases, Ce variation is positively correlated with Th variation and anticorrelated with Y variation (Fig. 9a). U correlates positively with Y and negatively with Ce (Fig. 9c). An extreme-rim alteration zone (cf. Fig. 5a) is present rimward of the high-Y band in Fig. 9d.

Some monazite grains (Fig. 9e–h) display zoning patterns that contrast with the anticorrelated (Th, Ce)–(Y,U) two-domain model. The grain shown in Fig. 9e–h displays four (or six) distinct compositional domains; (1) a high-Ce core (and two high-Ce "islets" outboard), (2) a slightly Th-enriched (relative to the core) outboard

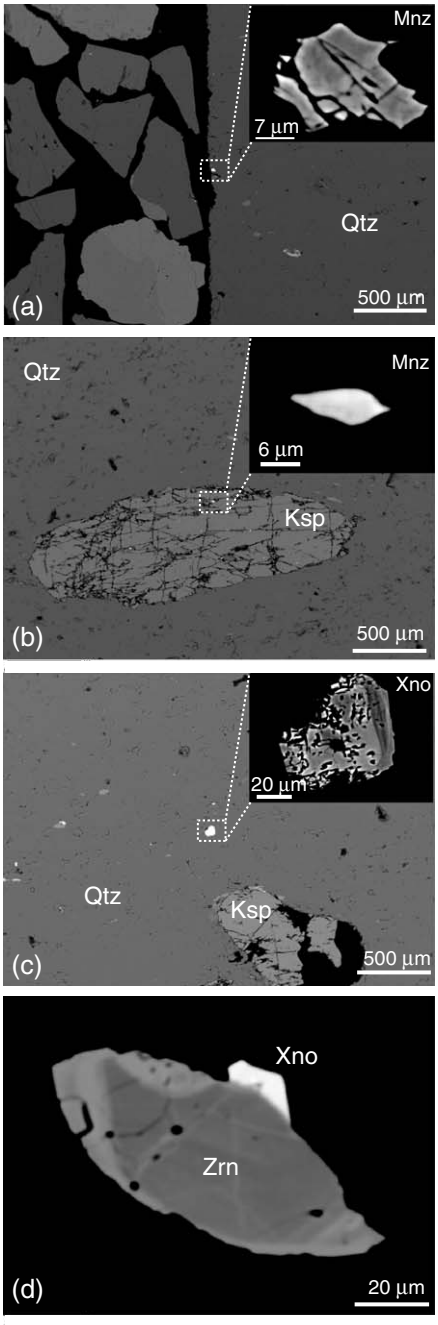

Fig. 6. BEI contrast images of accessory minerals in metaquartzite (sample Zch1a). (a) Monazite. Grain fragments at left of panel are not part of the thin section. (b) Monazite inclusion in flattened K-feldspar pebble. (c) Zoned, possibly detrital, xenotime. (d) Authigenic xenotime overgrowth on detrital zircon. Scale indicated at base of each panel.

(with an "islet" of this domain in the high-Ce core), and (3) a low-Th and low-U strip that is truncated by (4) a high (Th,U) rim containing a thorite inclusion. In this grain, Th and U are positively correlated in domains 2, 3, and 4. High-Y bands partially rim domain 1, and form a separate subdomain within domain 2; this subdomain has no recognizable equivalent in Ce, Th or U distribution within domain 2.

Complex compositional zoning of monazite requires that the compositional data be scrutinized for trends that may delimit distinct compositional groups, where such trends may not be obvious from compositional maps, or obscured by complex zoning. Th content is akin to a "fractionation indicator", since monazite partitions Th more strongly than most coexisting phases (Bea, 1996). There is general (albeit discontinuous) core-to-rim increase in Th concentration and Th/U ratio in monazite from sample Yhga. Y content of monazite is both a temperature monitor (Gratz and Heinrich, 1997; Pyle et al., 2001; Seydoux-Guillaume et al., 2002) and a garnet-growth monitor (Pyle and Spear, 1999; Pyle et al., 2001; Foster et al., 2004; Gibson et al., 2004). Absolute and normalized Y vs. Th variation are therefore useful compositional discriminants, and their application to thermometry and age analysis is demonstrated below.

Analyses of zoned matrix xenotime (Zch), xenotime overgrowth on zircon (Zch), and oriented xenotime inclusions in apatite (Yhfg1b, Yhga1a) are presented in Table 5. Mole fraction of Y+HREE is greater than 98.5% for all xenotime analyses, and xenotime HREE/Y ranges between 0.17 and 0.24. For the zoned xenotime matrix grain in Zch (Fig. 6b), decreased BEIC in the rim region is due to lower actinide content relative to the xenotime core.

7. Temperature estimates

7.1. Two-pyroxene thermometry

Samples Zch and Yhga do not contain mineral assemblages amenable to Fe–Mg exchange thermometry. Fe-augite and Fe-hornblende are present in charnockite (sample Yhfgwb), but do not represent an equilibrium mineral pair. The only texturally equilibrated Fe–Mg mineral pair observed in this sample suite is orthopyroxene–augite pairs in opdalite (sample Yhfg1).

Both pyroxenes contain exsolution lamellae (Fig. 10); orthopyroxene contains augite lamellae (Fig. 10e), and augite contains coarse orthopyroxene lamellae plus 2 sets of fine pigeonite lamellae (Fig. 10b). Area percent estimates of pyroxene host and lamellae are calculated using image threshold techniques (Fig. 10a, c), and reintegrated orthopyroxene and augite compositions are calculated (Fig. 10f) with the host and lamellae compositions listed in Table 6.

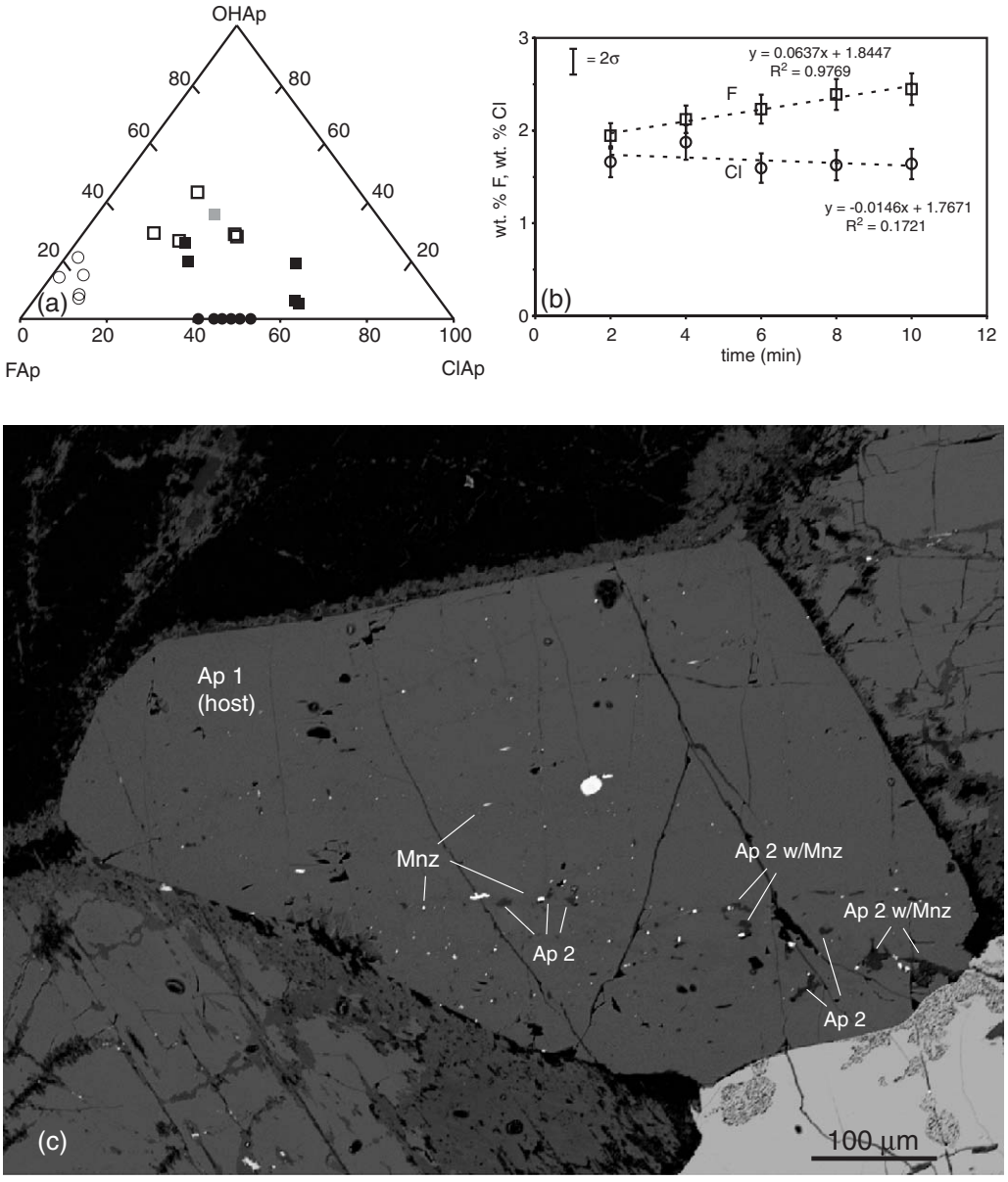

Fig. 7. Apatite composition. (a) Barycentric plot of F-, Cl-, and OH-apatite mole fractions. Open circles = sample Yhfg1b, solid circles = sample Yhfg1c, open squares = sample Yhfa1a, apatite inclusions in garnet, solid black squares=sample Yhfa1a, matrix apatite, solid gray square = sample Yhfa1a, metasomatized matrix apatite. (b) Time-series analysis of apatite performed to correct for F and Cl volatilization. Spots are analyzed in quintuplicate and regressed to determine zero-time F and Cl concentration. (c) Primary matrix apatite (Ap 1), sample Yhfg1c, with internal metasomatic domains of monazite spatially associated with darker, secondary apatite (Ap 2). Secondary apatite is enriched in FAp component and depleted in ClAp component relative to primary apatite.

Application of the two-pyroxene thermometer of Lindsley and Andersen (1983), using the component projection scheme of Spear and Markussen (1997), to the reintegrated pyroxene yields 1-atm temperatures of 900 °C for reintegrated augite, and 915 °C for reintegrated orthopyroxene. No estimates of emplacement pressure exist for the plutonic suite of the Upland; and T correction to an assumed emplacement pressure is speculative. However, crystallization of an amphibolitic, H_2O-rich melt at $P = 0.5$ GPa produces a crystallization sequence similar to the diorite–anorthositic diorite–dioritic anorthosite–anorthosite sequence of the Honey Brook anorthosite (Crawford et al., 1971). A pressure correction to 0.5 GPa assumes a shallow-to-moderate (~15–17 km) emplacement depth for the Honey Brook anorthosite and associated felsic plutonic

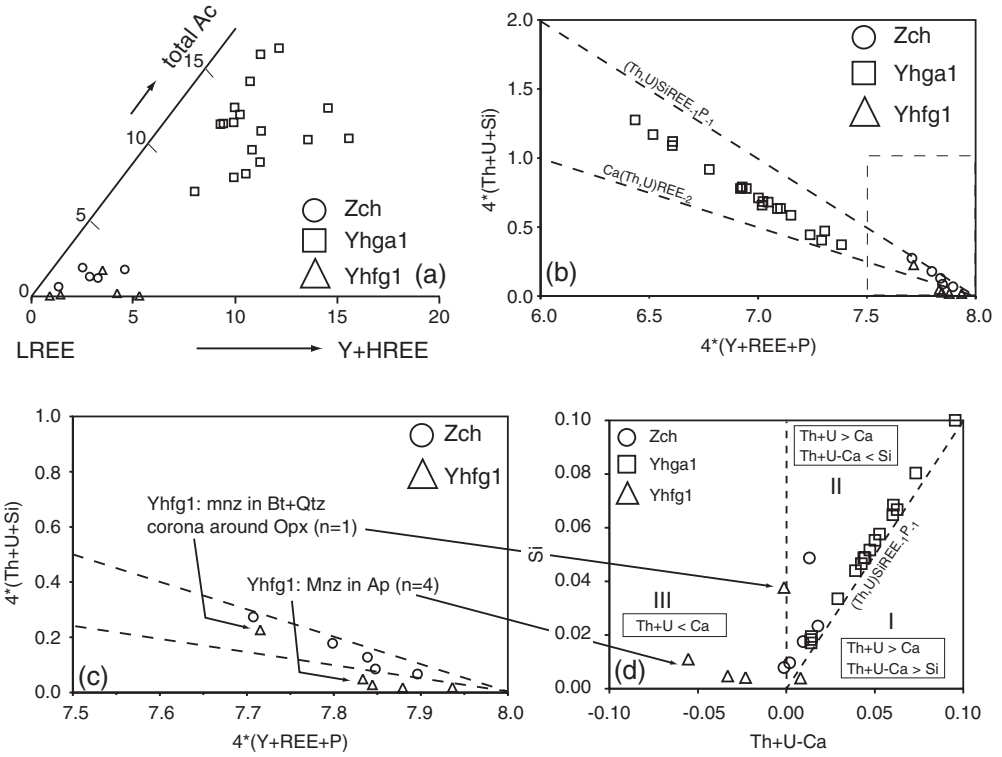

Fig. 8. Exploded monazite ternary LREE-(Y+HREE)-total actinide mole fraction plot. LREE apex is shown in detail. Primary monazite in felsic gneiss (Yhga1a, Yhga1b) is Th- and (Y+HREE) enriched relative secondary monazite in opdalite (Yhfg1b, Yhfg1c) and metaquartzite (Zch). (b) Plot of 4*(REE+Y+P) vs. 4*(Th+U+Si), monazite, with brabantite and huttonite component exchange vectors indicated. Monazite in Yhga shows significant huttonite component. (c) Expanded view of (c), showing detail of exchange vectors operating in monazite in samples Zch, Yhfg1b. (d) Actinide charge-balance plot. Monazite from Yhga and Zch plot essentially on brabantite exchange vector. Secondary monazite in Bt+Hbl corona and secondary monazite in apatite (triangles, sample Yhfg1b) plot off of the brabantite exchange vector, and are compositionally distinct in terms of Si content.

rocks, and yields pressure-corrected temperatures of 918 (augite) and 943 °C (orthopyroxene).

7.2. Accessory-phase thermometry (monazite–xenotime, monazite–garnet, garnet–xenotime)

The application of accessory phase thermometers offers an alternative means to retrieve equilibration temperatures when major phase mineral assemblages of the investigated samples are not amenable to commonly used geothermometers. Moreover, the existence of multiple accessory phase parageneses with a single sample allows for the potential retrieval of two or more growth temperatures along the rock's *P–T* path.

Accessory phase thermometers applicable to the HBU and CVS rocks are garnet (YAG)–monazite (Pyle et al., 2001), garnet (YAG)–xenotime (Pyle and Spear, 2000), and monazite–xenotime (Gratz and Heinrich, 1997; Seydoux-Guillaume et al., 2002). The garnet–monazite thermometer is used to obtain garnet–monazite equilibration temperatures in sample Yhga1, and the garnet–xenotime thermometer is used to obtain an independent estimate of garnet growth temperatures in the same sample. The monazite–xenotime thermometer is used to obtain equilibration temperatures for: 1) texturally secondary monazite–xenotime pairs in samples Yhfg1 and Yhga1; 2) monazite–xenotime pairs in sample Zch, and; 3) high-Y monazite cores in sample Yhga1.

Application of YAG (Yttrium Aluminum Garnet)–xenotime thermometry returns growth temperatures for garnet equilibrated in a xenotime-bearing mineral assemblage (Pyle and Spear, 2000). The empirical calibration of this thermometer demonstrates that the mole fraction of $Y_3Al_2Al_3O_{12}$ of garnet in equilibrium with xenotime decreases with decreasing temperature. If xenotime is absent from the mineral assemblage, YAG–xenotime temperatures are *minimum* temperature estimates. An exception to this rule arises in migmatitic samples, where melting of Y-bearing phosphates (Pyle and Spear, 1999) combined with large values of $D^{Y}_{Grt\text{-}Melt}$ may result in extreme Y enrichment

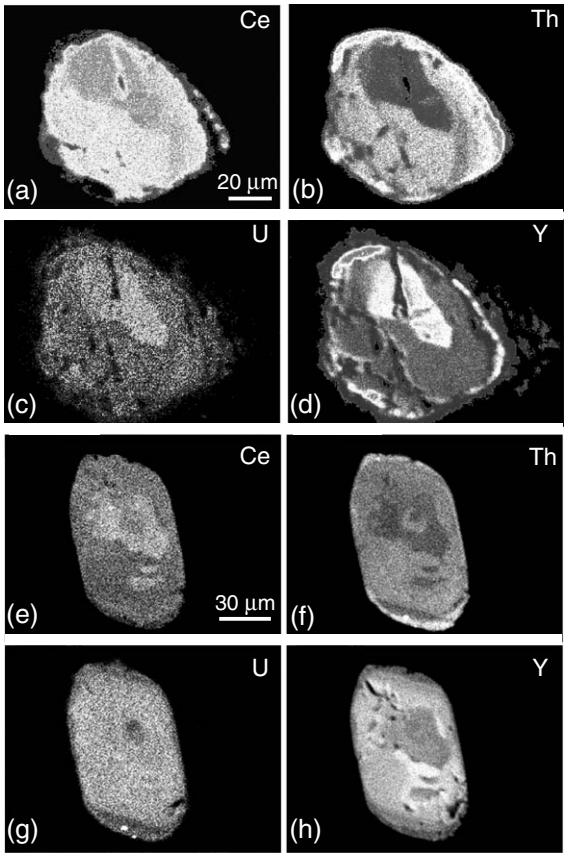

Fig. 9. Representative monazite Ce (a, e), Th (b, f), U (c, g), and Y (d, h) maps from sample Yhga1b, grains 12 (a–d) and 6 (e–h). Scale bars shown in panels (a) and (e). BEIC images of the same monazite grains are shown in Fig. 5.

(>2000 ppm) of anatectic garnet. Consideration of garnet textures and chemical zoning is generally, but not always, sufficient to distinguish anatectic garnet from subsolidus garnet (Spear and Kohn, 1996), and production of elemental markers for anatectic garnet requires a sufficient concentration of the given element in the sample, along with aforementioned large $D^{Y}_{Grt\text{-}Melt}$ values.

$X_{Y_3Al_2Al_3O_{12}}$ of the two analyzed garnet grains has limited core–rim variability (1230–930 ppm, X_{YAG}= 0.0017–0.0013), and application of the YAG-xenotime thermometer yields a correspondingly limited core–rim range of garnet growth temperatures (523 ± 14 to 535 ± 16 °C, Table 7). These temperature estimates are minimum estimates, as xenotime is not observed to be in textural equilibrium with garnet. However, xenotime inclusions in apatite suggest that the effective sample a_{YPO_4} was, at some point in the paragenesis, at xenotime saturation. Recovery of higher garnet growth temperatures may be hampered by garnet resorption, which is inferred from chloritized garnet rims and mantles of epidote+muscovite surrounding garnet (e.g., Fig. 3f).

In contrast with garnet, monazite equilibrated in a xenotime-bearing mineral assemblage shows increasing (Y+HREE) component with increasing temperature (e.g., Gratz and Heinrich, 1997). (Y+HREE) component vs. actinide component in monazite for sample Yhga1 is shown in Fig. 11a. Excluding the analysis of the altered rim, two compositional trends are present. Monazite core analyses show a weak positive correlation (R^2=0.17) between (Y+HREE) and actinide component, whereas analyses of monazite overgrowths show a moderate negative correlation (R^2=0.60) between (Y+HREE) and actinide component. Monazite is not observed as an inclusion in garnet in either Yhga1a or Yhga1b, but the sole monazite observed as inclusion in a porphyroblastic phase (perthitic K-feldspar) does not possess a low-Y overgrowth. This fact, and the observation that growth of garnet depletes the sample's effective Y bulk composition via fractionation of Y into garnet cores (Pyle and Spear, 1999) lead to the deduction that monazite cores grew pre- to syn-garnet, whereas the Y-depleted overgrowths likely grew syn- to post-garnet. Mnz–Grt thermometry may be applied to both monazite domains to infer which, if either, monazite domain equilibrated with garnet.

Application of garnet–monazite thermometry requires input of garnet, apatite, plagioclase, and monazite compositions (Table 7). No pressure estimates exist for amphibolite-facies felsic gniess, and the peak mineral assemblage (garnet+quartz+plagioclase+K-feldspar+ilmenite) is not amenable to geobarometry. The paucity of garnet in HBU *mafic* schists implies lower pressures of Grenvillian metamorphism than the 0.8–0.9 GPa estimated for mafic gneisses of the West Chester Massif (Wagner and Crawford, 1975). Therefore, a pressure of 0.5 GPa is assumed for all thermometry calculations, and f_{H_2O} is calculated at 0.5 GPa for T values ranging between 500 and 650 °C and X_{H_2O} between 0.7 and 1.0. Plagioclase composition is essentially constant at An_{17}, and grossular content of garnet ranges from 3 to 4 mol%. For the temperature calculations, X_{grs} is varied between 0.03 and 0.04, with the following compositional pairings: 1) garnet core (black squares, Fig. 11b): garnet composition is fixed at 0.0017 X_{YAG}, X_{OHAp} is varied between 0.30 and 0.25 (range of compositions for apatite included in garnet), and X_{YPO_4}, Mnz is fixed at 0.0399, which is the lower compositional limit of the monazite core domain analyses; 2) garnet rim (gray squares, Fig. 11b): garnet composition is fixed at 0.0013 X_{YAG}, X_{OHAp} is varied between 0.20 and 0.08 (range of compositions for

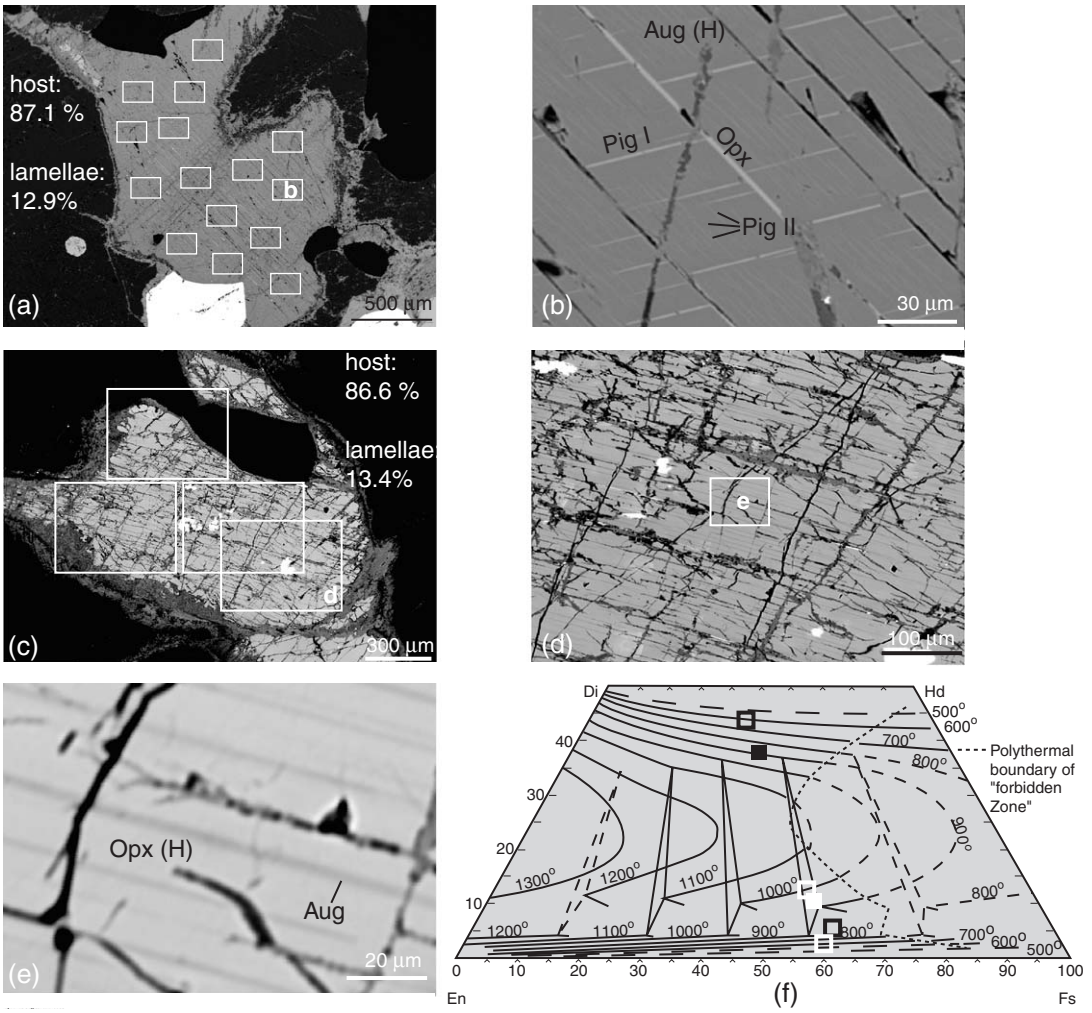

Fig. 10. Reconstitution of primary pyroxene using image analysis. (a) Augite grain containing three generations of exsolution lamellae. Image thresholding of host and lamellae performed for each image box shown in (a), an example of which is shown in detail in (b). (c) Orthopyroxene grain containing augite lamellae. Image thresholding of host and lamellae performed for each image box shown in (c), an example of which is shown in detail in (d). (e) Enlargement of image in (d), showing scale of augite lamellae. (e) 1-atm, polythermal graphical thermometer of Lindsley and Andersen (1983), with pyroxene compositions from sample Yhfg 1b. Open symbols=host and exsolved phase; solid symbols=reconstituted phase. Black=augite host+opx and pigeonite exsolution. White=orthopyroxene host and pigeonite exsolution. Reconstituted pyroxenes corrected to $P=0.5$ GPa yield temperatures of 915 (augite) and 943 °C (pigeonite).

matrix apatite), and X_{YPO_4}, Mnz is fixed at 0.0525, which is the median composition of the monazite core domain analyses. The entire compositional range of the monazite core domain is not used, as YAG–xenotime thermometry indicates that the analyzed garnets grew over a restricted temperature interval that was likely smaller than the temperature interval over which the core domain of monazite grew.

For the above pairings, thermometry returns a monazite–garnet equilibration temperature range of 489 ± 50–511 ± 50 °C for the garnet core composition pairings, and 512 ± 50–544 ± 50 °C for the garnet rim composition pairings. This latter temperature range overlaps the YAG–xenotime temperature estimates for garnet growth. If the most Y-rich monazite (Table 4, monazite analysis b-6) is paired with the garnet rim composition, a Mnz–Grt equilibration temperature of 558 ± 25 °C is returned.

To assess the possibility that garnet was *not* in equilibrium with the monazite cores, monazite–xenotime equilibration temperatures are calculated (Table 7) using the mole fraction of (Y+HREE), Mnz (for the equivalent value of X_{YPO_4} used in the garnet–monazite thermometer), and the empirical thermometer calibration of Pyle et al. (2001), plus the experimental calibrations of Gratz and Heinrich (1997) and Seydoux-

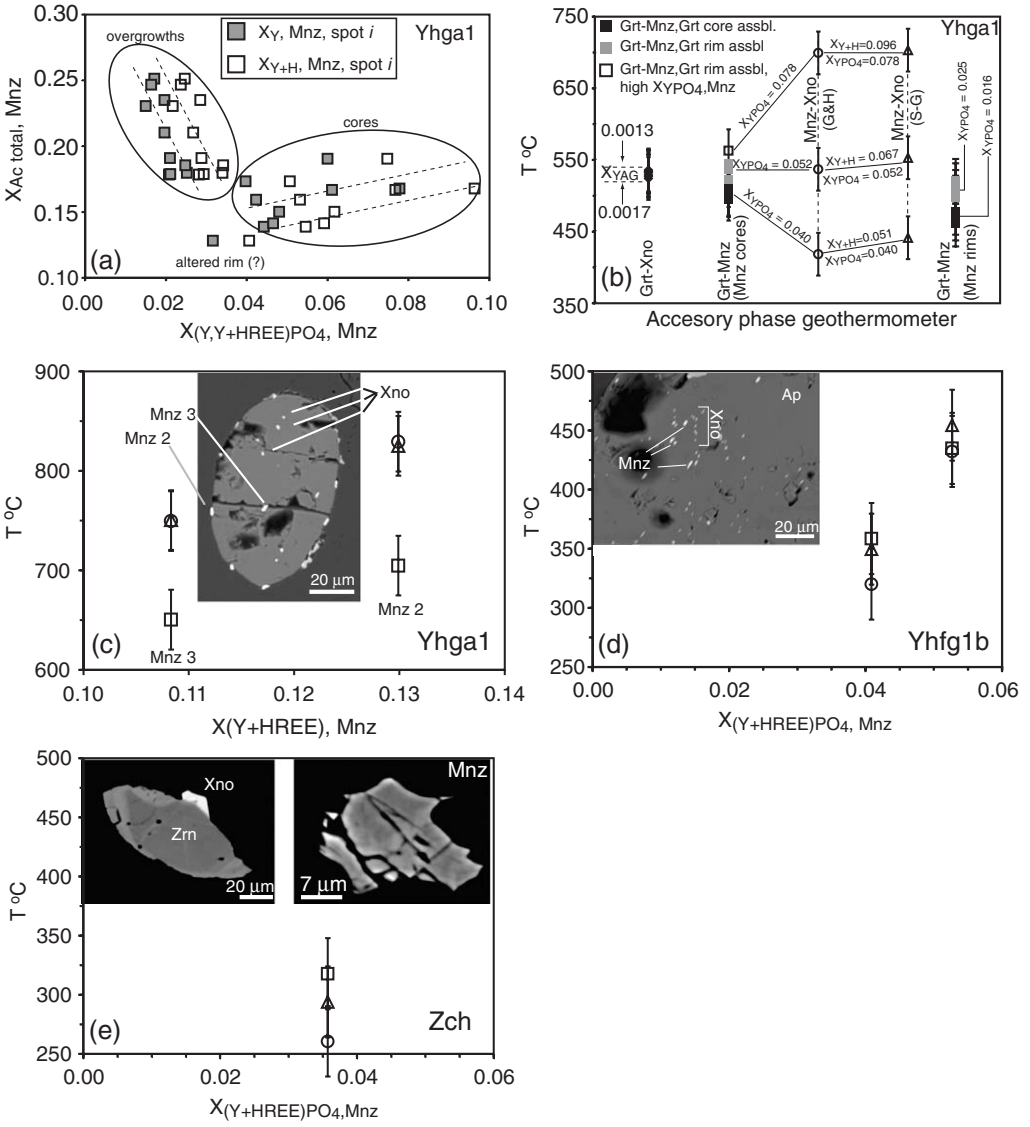

Fig. 11. Summary figure for monazite–xenotime–garnet thermometry, samples Yhga1, Yhfg1, and Zch. (a) Plot of mole fraction (Y+HREE) vs. mole fraction Th, sample Yhga1. Two trends are discerned; cores with a weak positive correlation between Y+HREE and Th, and overgrowths with a strong Y+HREE-Th anticorrelation. An altered rim of monazite (labeled) contains both low Th and low (Y+HREE). Monazite cores are interpreted to record early, prograde metamorphism of the amphibolite-facies felsic gneisses, which either pre-dated or overlapped garnet growth. Mole fraction of both $X_{Y,\ Mnz}$ (solid gray squares) and $X_{(Y+HREE),\ Mnz}$ (open squares) is plotted for each spot analysis. (b) Monazite–xenotime–garnet thermometry, sample Yhga1. Plot shows temperature estimates from YAG–xenotime thermometry (Pyle and Spear, 2000), YAG–monazite thermometry (Pyle et al., 2001), and the monazite–xenotime thermometer calibrations of Gratz and Heinrich (1997) and Seydoux-Guillaume et al. (2002). Two sets of garnet–monazite temperatures are calculated for garnet-core mineral assemblages and garnet-rim mineral assemblages. The first set assumes garnet is in equilibrium with monazite core domain only. The second set assumes that garnet is in equilibrium with the monazite rim domain only. Monazite–xenotime temperature estimates (Gratz and Heinrich, 1997; Seydoux-Guillaume et al., 2002) are calculated using core domain $X_{(Y+HREE)PO_{4,\ Mnz}}$ values corresponding to the $_{XYPO_4}$, Mnz values used for garnet–monazite thermometry. The highest values of $X_{(Y+HREE)PO_{4,\ Mnz}}$ give significantly higher Mnz–Xno temperatures than the corresponding Mnz–Garnet temperatures, suggesting that monazite cores did not equilibrate with garnet. (c) Temperature estimates for monazite+xenotime inclusions in apatite, sample Yhga1. (d) Temperature estimates for monazite and xenotime inclusions in apatite, sample Yhfg1b. (e) Temperature estimates for monazite+authigenic xenotime, sample Zch. For (c, d, e), squares=Pyle et al. (2001) calibration, circles=Gratz and Heinrich (1997) calibration, triangles=Seydoux-Guillaume et al. (2002) calibration.

Guillaume et al. (2002). The temperature range calculated for the range of $X_{(Y+HREE)PO_4}$, Mnz in the monazite core domain is 417–699 (Gratz and Heinrich) and 440–703 °C (Seydoux-Guillaume et al., 2002), with a smaller temperature range (424–616 °C) returned from the Pyle et al. (2001) calibration.

Oriented monazite and xenotime inclusions in apatite, sample Yhga1, are in textural equilibrium (Fig. 5i), and monazite has high $X_{(Y+HREE)PO_4}$ (0.11–0.13). Application of monazite–xenotime thermometry to such monazite–xenotime pairs yields equilibration temperatures of 650–705 °C for the empirical calibration and 750–830 °C for the experimental calibrations (Fig. 11c). These temperatures are significantly higher than matrix monazite core-equilibration temperatures, and the reaction of apatite to form monazite + xenotime may record the thermal culmination of the same episode in which the cores of matrix monazite grew, or may represent a second, separate, high-temperature event. Peak temperature estimates from monazite core + xenotime thermometry are comparable to peak temperature estimates of 680 ± 40 °C obtained by graphite–calcite $^{13}C/^{12}C$ exchange thermometry (Crawford and Valley, 1990) for correlative samples.

High peak Mnz–Xno temperatures returned by monazite cores (650–700 °C), as compared to the lower temperatures returned by garnet–monazite core compositional pairings (490–560 °C), suggest that the monazite cores did not equilibrate with a garnet-bearing mineral assemblage. Garnet–monazite thermometry pairing garnet compositions with those of the low-Y, high-Th monazite overgrowth domain ($0.0157 \leq X_{YPO_4} \leq 0.0253$) yields equilibration temperatures of 464–481 °C for the garnet core and 497–520 °C for the garnet rim (Fig. 11b). These temperatures are lower than garnet–monazite core temperatures, and suggest that monazite overgrowths did not equilibrate with surviving (i.e., non-resorbed) garnet.

Application of accessory phase thermometry in all other samples is relatively straightforward, as the monazite–xenotime pairs appear to be in textural equilibrium (Fig. 4), or at least coexisting in the sample matrix (Fig. 6a, c, d). These parageneses include monazite–xenotime inclusions in apatite (sample Yhfg1b, Fig. 11d), and monazite–xenotime pairs in sample Zch (Fig. 11e). Two monazite analyses and one xenotime analysis from Yhfg1b yield (± 50 °C 2σ) temperatures of 358 (Pyle et al., 2001), 320 (Gratz and Heinrich, 1997) and 349 °C (Seydoux-Guillaume et al., 2002) for the first Mnz–Xno pair, and 434, 432, and 454 °C for the second Mnz–Xno pair (Fig. 11d). Despite the textural similarities between samples Yhfg1 and Ygha1, the apatite-hosted monazite–xenotime formation event in Yhfg1b records significantly lower T than the Mnz–Xno formation event recorded by sample Yhga1 (Fig. 11c).

One monazite–xenotime pair from Zch yields equilibration temperatures of 318 (Pyle et al.), 261 (Gratz and Heinrich), and 294 °C (Seydoux-Guillaume et al.) (Fig. 11e). These temperatures are consistent with conditions of grennschist-facies metamorphism reported for the Chester Valley metasediments (Crawford and Crawford, 1980, Crawford and Hoersch, 1984).

8. Th–U–total Pb Electron Microprobe Analyzer (EMPA) ages

Th–U–total Pb EMPA spot analyses (dates) are presented in Table 8. Dated samples include Yhfg1b, Yhga1a, Yhga1b, and Zch1a. 1σ compositional uncertainties are listed for Th, U, and the 2 independent determinations of Pb. Single-spot 1σ date uncertainties determined by Monte Carlo propagation of analytical uncertainties through the age equation of Montel et al. (1996) are listed, as well.

8.1. Yhga1 (samples a and b)

Atomic Ce/Y vs. atomic Th/U delineates monazite core and monazite overgrowth domains (Fig. 12), and a near-rim alteration domain (Fig. 12) is also compositionally distinguishable. The 61 spot analyses (122 dates) were classified a priori into compositional core, overgrowth, and “altered rim” domains, independent of date determination.

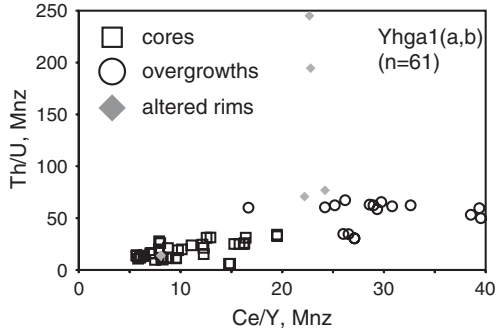

Fig. 12. Plot of atomic Ce/Y (Mnz) vs. atomic Th/U (Mnz), samples Yhga1a and Yhga1b. The 61 spot analyses (122 dates) are discriminated by texture and composition (low (Ce/Y, Th/U) cores, high (Ce/Y, Th/U) overgrowths, and mechanically altered rims). This discrimination is used for a priori classification monazite domains (see Fig. 13).

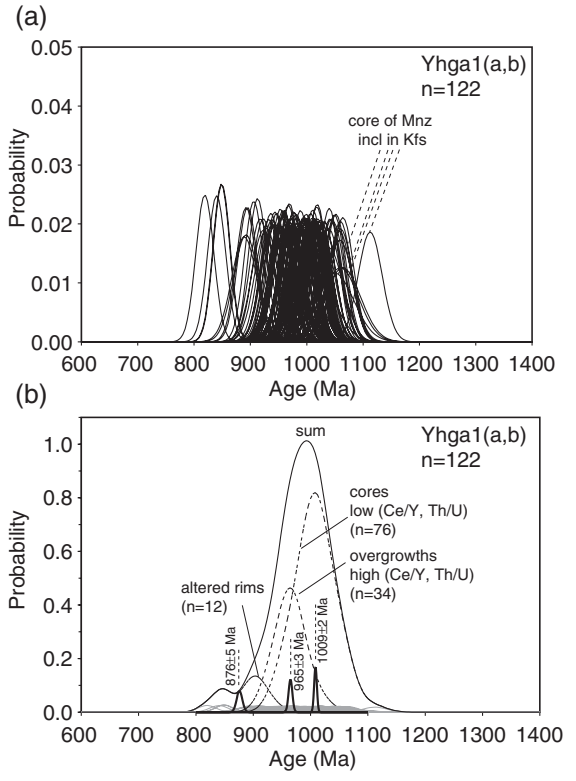

Fig. 13. Monazite age distribution diagram, samples Yhga1a and Yhga1b. (a) Individual dates ($n=122$) represented as a Gaussian distribution about the mean age and propagated age uncertainty. Age uncertainty on each determination is calculated by Monte Carlo propagation (10,000 trials) of 1-sigma U, Th, and Pb analytical uncertainties through the U–Th–total Pb age equation of Montel et al. (1996). Analyses of the core of monazite included in K-feldspar indicated. (b) Pseudo-Gaussian weighted probability curves for all analyses (sum) and the three compositionally delimited monazite domains (dashed black curves). The weighted mean and associated standard error of each domain are also represented as a Gaussian distribution (thick solid black curves). The individual measurements plotted in (a) are shown in (b) as gray Gaussian curves.

One hundred twenty-two dates from Yhga1 are plotted as Gaussian distributions, with standard deviations corresponding to age uncertainties derived through Monte Carlo propagation of analytical uncertainties. The dates cluster about 1000 Ma, with one noticeably older determination, and a group of younger dates between 800 and 900 Ma. The older age determination (Table 8, #5/3/1, #5/3/2) is the low-Th (~3.3 wt.%) core of the only monazite observed as an inclusion in K-feldspar (Fig. 13a). The individual dates are separated into their respective domains (Fig. 13b), and the approximate mean age and distribution of each domain are indicated by the cumulative sum Gaussian, or pseudo-Gaussian histogram (dashed line). For each domain, the Th–U–total Pb EMPA weighted average age and two standard errors are 1009 ± 4 (high-Y cores, $n=76$), 965 ± 6 (high-Th overgrowths, $n=34$), and 876 ± 10 Ma (altered rims, $n=12$).

As a comparative test on the robustness of the compositional discrimination of age domains, the minimum number of statistically independent age domains is calculated using the method of Wendt and Carl (1991). This method also retrieves 3 statistically independent age domains for sample Yhga1: 1020 ± 6 (cores), 962 ± 6 (overgrowths), and 870 ± 10 Ma (altered rims). The latter two statistically determined age domains are indistinguishable (Fig. 14) from the high-Th overgrowth domain and the altered rim domain. The oldest statistically determined domain is significantly older than the compositionally determined mean age, but is within the uncertainty of a single-spot analysis (Fig. 14). Overall, there is excellent correspondence between the compositionally determined domain mean ages and their statistically determined equivalents.

8.2. Yhfg1b

Age analyses of monazite inclusions in apatite are indeterminate, due to extremely low Th, U and Pb concentrations. However, texturally secondary monazite included in a zircon rim (Fig. 4f), and monazite in a biotite+hornblende corona around orthopyroxene (Fig. 4g) yield statistically distinguishable dates (Fig. 15a). Due to small sample size and compositional disparity between the 2 monazite grains, both discrimination methods yielded identical results. The high-Th monazite inclusion in zircon yields a weighted average Th–U–total Pb age of 714 ± 24 Ma, and the low-Th monazite

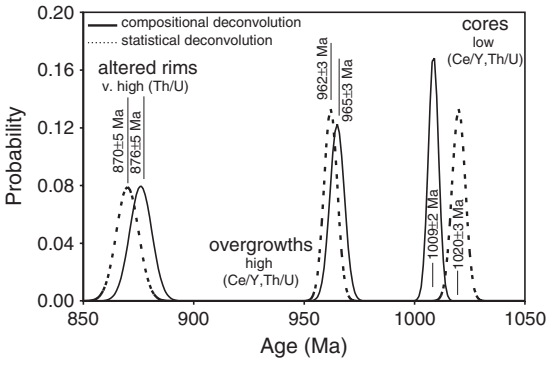

Fig. 14. Comparison of the three mean domain ages, sample Yhga1(a,b), as determined by textural and compositional discrimination (solid black Gaussian curves) and statistical deconvolution (dashed black Gaussian curves) according to the method of Wendt and Carl (1991) and Montel et al. (1996). Statistical core domain mean age is 20 m.y. older than the compositionally determined core domain mean age, but the mean ages of the other two domains as calculated by both methods are statistically indistinguishable.

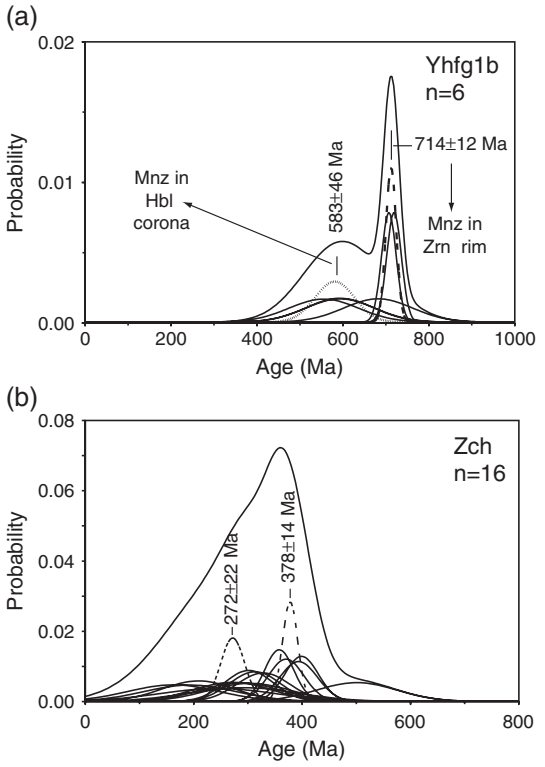

Fig. 15. Monazite age distribution diagram, samples Yhfg1b (a) and Zch1a (b). No compositional evidence for classification of a priori monazite domains was found for either sample. Statistical deconvolution yields two distinct age domains for Yhfg1b of 714 ± 24 Ma (2 s.e.) for monazite in altered zircon rim, and 583 ± 92 Ma (2 s.e.) for monazite in a Bt+Hbl corona around Opx. Sample Zch1a fails the statistical test for a single age domain at 345 ± 24 (2 s.e.), and yields two age domains centered on 378 ± 28 (2 s.e.) and 272 ± 44 (2 s.e.).

monazite inclusion in the corona gives a weighted average Th–U–total Pb age of 583 ± 92 Ma.

8.3. Zch (Chickies Quartzite)

Monazite in Zch yields 16 dates; no compositional discrimination is possible due to the lack of monazite compositional variation. Statistical deconvolution on this small dataset generates two independent age domains (Fig. 15b), one at 378 ± 28 Ma (n = 6), and the other centered at 272 ± 44 Ma (n = 10). The older domain is slightly skewed by a single date at 501 ± 148 Ma, but, overall, the results indicate a monazite population produced by Paleozoic metamorphism rather than inheritance of Grenvillian detrital monazite.

9. Discussion

This study has emphasized: 1) the importance of textural recognition and classification of multiple accessory phases parageneses within a single sample, and correlation of major phase and accessory phase parageneses; 2) the potential for compositionally based discrimination of multiple age domains in complexly zoned monazite. Such discrimination, in conjunction with major phase reaction analysis, is also useful in determining the appropriate accessory phase geothermometer(s) to apply to individual parageneses. Within this analytical context, a number of conclusions about the thermal and tectonic history of the Honey Brook Upland Chester Valley Sequence can be made.

9.1. P–T–t conditions of Grenvillian plutonism, volcanism, and metamorphism

Textural and compositional analysis of anorthosite–cognate felsic to intermediate gneisses from the Honey Brook Upland indicates that the "granulite-facies" samples Yhfg1, and Yhfgwb are likely plutonic in origin; this observation is borne out by the 2-pyroxene thermometry temperatures (915–945 °C) derived from reintegration of host+exsolved ortho- and clinopyroxene (Fig. 10). Zircon U–Pb age determinations for both the anorthosite and co-genetic plutonic rocks of the Honey Brook Upland are lacking, so no direct correlation to dated Grenville Anorthosite–Mangerite–Charnockite–Granite (AMCG) intrusives such as the Marcy Anorthosite suite (1154 ± 6 Ma, McLelland et al., 2004), or the younger, more southerly Montpelier (VA) anorthosite (1045 ± 10 Ma, Aleinikoff et al., 1996) is possible. Zircon in samples from the Avondale–West Chester Massif (Fig. 1), to the south of the Upland, yields U–Pb ages of 1050–980 Ma (Grauert et al., 1973), which overlap the monazite ages from sample Yhga.

Likewise, no age determinations have been made on oscillatory-zoned (and presumably igneous) zircon found in amphibolite-facies quartzofeldspathic gneiss (Yhga) or mafic gneiss of either amphibolite- or granulite-grade. The protolith of the granulite-facies mafic gneiss is basalt (Crawford et al., 1999) and the suite of amphibolite-facies gneisses (Yhma, Yhia, Yhfa, Yhga) possess bulk-compositional affinities to subalkaline and "normal" to "K-poor" Cascade and Aleutian volcanics (Irvine and Baragar, 1971), which lead Crawford and Hoersch (1984) to propose volcanic or volcaniclastic protoliths for these units. The high actinide (10–20 mol%) component of monazite from Yhga (Table 5), combined with the dominance of the huttonite exchange vector over the brabantite exchange vector (Fig. 8b, d) suggests a high-temperature igneous source material for the monazites (Broska et al., 2000).

Petrologic evidence presented above suggests that the metamorphic events affecting the Honey Brook Upland subsequent to AMCG intrusion and calc-alkaline volcanism were largely amphibolite-facies, with metamorphic intensity increasing continuously from south to north, as proposed by Crawford and Hoersch (1984). The pyroxene-bearing assemblages (hypersthene+augite in Yhfg1, ferroaugite in Yhfgwb) are igneous in origin, and the metamorphic overprint preserved in these samples is of upper-amphibolite-facies, as indicated by coronal overgrowths of Cl-bearing (1.5–2.5 wt.%) K-hornblende in Yhfgwb, and the coronal structure orthopyroxene (FM=60)–cummingtonite–quartz+calcite+biotite–biotite+Cl-bearing (0.5–1.5 wt.%) K-hornblende (Fig. 3d). This coronal texture suggests the reaction sequence (in CaKMASH(CO_2))

$$3.5\ Mg_2Si_2O_6 + SiO_2 + H_2O = Mg_7Si_8O_{22}(OH)_2 \quad (1)$$

$$0.75\ Mg_7Si_8O_{22}(OH)_2 + 1.75\ KAlSi_3O_8 + H_2O = 1.75\ KMg_3AlSi_3O_{10}(OH)_2 + 3.375\ SiO_2 \quad (2)$$

$$0.167\ Mg_7Si_8O_{22}(OH)_2 + 0.583\ SiO_2 + 0.167\ KAlSi_3O_8 + 0.5\ KMg_3AlSi_3O_{10}(OH)_2 + 0.333\ CaAl_2Si_2O_8 + CaCO_3 = 0.667\ KCa_2Mg_4Al_2Si_6O_{22}(OH)_2 + CO_2 \quad (3)$$

The lower stability boundary of Opx+Cum+Qtz is 730±10 °C (0.29 GPa) and 740±10 °C (0.5 GPa) (Fonarev and Korolkov, 1980), and yields an upper limit for metamorphism of the HBU intrusive units. This metamorphism was accompanied by a mixed H_2O–CO_2–KCl fluid, as indicated by: 1) progress of reaction (1); 2) the presence of modal calcite; 3) the presence of Cl-apatite and Cl-bearing potassic ($K_{A\text{-site}} > Na_{A\text{-site}}$) hornblende. The temperature constraints from reactions (1)–(3) yield maximum *T*s not inconsistent with the "granulite-facies" peak *T* estimate of 750±40 °C returned by calcite–graphite isotope thermometry (Crawford and Valley, 1990).

For "amphibolite-facies" quartzofeldspathic gneisses (Yhga), the peak assemblage microcline+plagioclase+quartz+garnet± biotite+ilmenite indicates peak metamorphic temperatures above muscovite stability, but below the alkali feldspar solvus (e.g., Thompson and Tracy, 1979). These brackets peak *T* between ~650 and 725 °C (assuming *P* ~0.5 GPa). This is consistent with both monazite–xenotime thermometry for monazite core domains (620–700 °C) and 680±40 °C returned by calcite–graphite isotope thermometry (Crawford and Valley, 1990). High Th/U-monazite domains in Yhga grew in garnet- and xenotime-absent mineral assemblage, precluding application of either monazite–garnet or monazite–xenotime thermometry. However, a discontinuous increase in Th/U of monazite has been shown to correlate with monazite growth during or subsequent to anatexis; uranium tends to partition into fluid or partial melts relative to restitic phases (Bea and Montero, 1999). U partitioning into a fluid phase is especially effective if Cl is available to complex tetravalent U (Peiffert et al., 1996). The composition of matrix apatite in Yhga is enriched in Cl relative to apatite included in garnet, indicating higher Cl content of the ambient fluid at this later stage of the sample paragenesis. Thus, the monazite overgrowth domain equilibrated with a Cl-rich fluid, accounting for the depletion of U from the monazite rim domain. Whether this fluid was aqueous or a silicate melt is unknown, but textural evidence for melting of the amphibolite-facies felsic gneisses is equivocal.

The Proterozoic portion of the *P–T–t* history of the HBU, synthesizing the information presented above (Fig. 16)), involved emplacement of the Honey Brook anorthosite and its cognate intrusives, along with calc–alkaline volcanism. Temperature of emplacement for the opdalite (Yhfg1) is estimated at 915–945 °C; emplacement pressure is unknown. Although primary magmatic zircon in the AMCG rocks and metavolcanics is undated, the AMCG emplacement and volcanism must predate the metamorphism; therefore, the crystallization age of the Honey Brook anorthosite and associated intrusives could correlate with the ~1155 Ma, age of the Marcy AMCG suite (McLelland et al., 2004), or the 1045±10 Ma crystallization age of the Montpelier anorthosite of the Goochland (VA) terrane (Aleinikoff et al., 1996).

As recorded by growth of metamorphic monazite in felsic volcanic protoliths (sample Yhga1a, Yhga1b), Grenvillian metamorphism affecting the Honey Brook Upland consisted of at least two high-*T* episodes, one between 1020 and 1010 Ma, and the other ca. 970–960 Ma. Peak temperatures for the 1020–1010 Ma metamorphism were on the order of 700 °C (monazite–xenotime thermometry). Peak temperatures for the 970–960 Ma metamorphism are unconstrained by thermometry, but the low Y concentration in monazite, and discontinuous increase in Th/U ratio in the monazite overgrowth domain suggests: 1) garnet growth occurred in the prograde stages of the 970–960 Ma metamorphism; 2) the culmination of the 970–960 Ma metamorphism involved significant growth of monazite with a character-

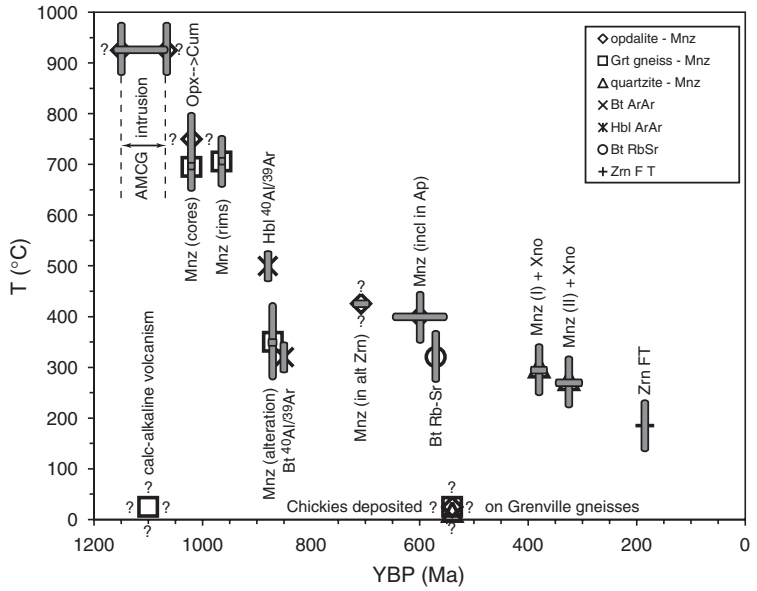

Fig. 16. Summary temperature–time plot for rocks in the Honey Brook Upland and Chickies Quartzite of the overlying metasedimentary Chester Valley Sequence. *T–t* data from monazite thermochronometry (this study), Hornblende and biotite Ar–Ar closure dates (Sutter et al., 1980), Biotite-whole rock Rb–Sr isochrons (Kohn et al., 1993), and Zircon fission-track ages (Kohn et al., 1993). Vertical gray bars indicated estimated 2σ temperature uncertainties. Age uncertainties for monazite are ±2 standard errors of mean domain age. Age uncertainties for Hbl Ar–Ar, Bt Ar–Ar, Bt Rb–Sr, and Zrn fission track data are smaller than plotting symbol width. Paired vertical or horizontal question marks indicated unconstrained temperature or age placement and uncertainty, respectively. ~0 °C temperatures are assumed for surface-exposed lithologies, such as Grenville-age calc-alkaline volcanics subsequent to eruption, and Grenville-age gneisses of the HBU, on which the Chickies Quartzite was directly deposited ca. 550 Ma. Honey Brook anorthosite–charnockite intrusion is placed between ~1155 and 1040 Ma by correlation with Adirondack AMCG intrusion (McLelland et al., 2004) and Montpelier (VA) anorthosite (Aleinikoff et al., 1996).

istic high-*T* signature; i.e., high Th (15–20 wt.%) coupled with high Th/U (~50) (Bea and Montero, 1999).

The 1020–1010 and 970–960 Ma metamorphic events are manifest in the plutonic rocks as coronal overgrowths of amphibole on igneous pyroxene, indicating fluid-assisted metamorphism. The estimated temperature of 730–740 °C (at 0.3–0.5 GPa) for the orthopyroxene+H_2O to cummingtonite reaction (Fonarev and Korolkov, 1980) is consistent with the observation that peak metamorphic temperatures were likely to be higher in the deeper-seated plutonic complex than in the overlying volcanogenic pile. Moreover, the evidence points to terrane-wide evolution of a more CO_2- and Cl-rich fluid by the later metamorphic pulse; the first generation of amphibole in the opdalite is a Cl-free cummingtonite, which is later replaced by Cl-bearing K-hornblende associated with calcite. Early apatite inclusions in garnet in the metavolcanics are depleted in Cl (X_{ClAp}=0.20–0.35) relative to later matrix apatite (X_{ClAp}=0.55–0.60).

The youngest monazite domain in Yhga (876 ± 10 Ma) is characterized by U depletion and very high Th/U values of 75–250, as compared to the average Th/U value of ~50 of the overgrowth domain. This domain is interpreted as resulting from low-*T* hydrothermal growth, a occurrence similar to that described by Poitrasson et al. (2000), where monazite grown during hydrothermal alteration of the Skiddaw granite at 260 ± 30 °C has a Th/U value of ~700. The growth of low-T (≥300 °C) monazite at 880–860 Ma is not inconsistent with $^{40}Ar/^{39}Ar$ closure ages of 880 and 850 Ma reported by Sutter et al. (1980) for hornblende (closure *T* 580–490 °C, Harrison, 1981) and biotite (closure *T* 310(±40)–330±(30) °C, Grove and Harrison, 1996), respectively, from the Honey Brook Upland. Moreover, the observation that the Ar–Ar closure temperatures were not later reset places constraints on subsequent Paleozoic metamorphism of the Honey Brook Upland.

9.2. Evidence for late (715–570 Ma) Proterozoic alteration of HBU rocks

Texturally secondary monazite is present in opdalite as oriented inclusions in apatite, as well as on altered zircon rims, and associated with hornblende coronas on orthopyroxene (Fig. 4). Monazite inclusions in apatite are too low in Th and U (Table 8, #c-12, d-14) to yield meaningful EMPA ages, but return monazite–xenotime equilibration temperatures of 320–430 °C (Table 7; Fig.

11d). The dateable secondary monazites yield Th–U–total Pb EMPA ages (Fig. 16) between 714 ± 24 (monazite associated with zircon) and 583 ± 92 Ma (monazite associated with hornblende).

This evidence for a low-*T* thermal event or events between 715 and 580 Ma may be related to incipient rifting of the Rodinian supercontinent and associated igneous activity. Catoctin-affinity (e.g., Smith and Barnes, 1994) ENE-WSW-trending basaltic dikes (with subordinate pegmatite) are abundant throughout the HBU (Fig. 2), have well-preserved chill-margins (Smith and Barnes, 1994) indicating shallow emplacement, and are presumably contemporaneous with diabase and felsic dikes (602 ± 2 Ma; Smith, 2003) found in the Reading Prong. The Honey Brook Upland is also known to have had a Neoproterozoic volcanic cover (MacLachlan, 1994, quoting Smith, pers comm., Marquez, pers comm), based on limited occurrences of volcaniclastic debris (chlorite + mica schists) at the base of the Chickies Formation.

Evidence for fluid infiltration during this low- to moderate-*T* thermal disturbance is given by oriented inclusions of monazite and xenotime in matrix apatite (Fig. 4h, i). Such oriented inclusions are interpreted to have formed during metasomatic alteration of the apatite. Harlov et al. (2002) and Harlov and Forster (2003) experimentally demonstrated that metasomatism of natural REE-bearing Cl-rich apatite by either H_2O-rich fluid or KCl-bearing brine results in formation of a new generation of Cl-poorer apatite plus monazite and xenotime. The range of temperatures over which Harlov et al. (2002) experimentally produced Cl-poor apatite plus monazite and xenotime by metasomatizing primary Cl-rich apatite is large (300–900 °C). Therefore, the equilibration temperatures returned by monazite–xenotime inclusions in apatite (325–425 °C) are not unreasonable. These temperatures support the interpretation of their formation during a low-*T* thermal disturbance that did not reset the more robust Ar–Ar systematics of biotite or hornblende present in HBU gneisses subject to Grenvillian metamorphism (Sutter et al., 1980), but that did disturb the Rb–Sr isotopic systematics of biotite in the HBU gneisses, which are much more sensitive to modest temperature increases (Faure, 1986). A Rb–Sr whole rock-biotite isochron age of 567 Ma (Fig. 16) for felsic gneiss from the HBU (Downingtown 7.5′ Quadrangle; Kohn et al., 1993) suggests biotite Rb–Sr resetting after a late Proterozoic (~600 Ma) thermal disturbance.

The diabase and pegmatite dikes, rare volcanic cover of the Honey Brook Upland, and the overlying Chickies Quartzite record the rift-to-drift transition accompanying the break up of the Laurentian eastern margin, and the formation of Iapetus during the latest Proterozoic to early Cambrian (Faill, 1997). It is proposed that the low-*T* metasomatic alteration recorded by secondary monazite in opdalite resulted from higher than normal heat flow (in thinned crust) and fluid circulation accompanying Neoproterozoic igneous activity in the HBU. Subsequent thermal uplift following the rift-to-drift transition eroded an unknown thickness of Neoproterozoic volcanic cover plus Grenville-age gneiss from the Honey Brook Upland, prior to deposition of the Chickies Quartzite. The monazite ages (Neoproterozoic) given above do not record a Paleozoic alteration of the opdalite. However, since low-grade Paleozoic metamorphism affected sediments of the Chester Valley sequence, the underlying basement rocks, including Mesoproterozoic "granulite"- and "amphibolite"-facies gneisses plus Neoproterozoic diabase, must have been affected, as well.

9.3. Paleozoic metamorphism of the Honey Brook Upland and cover sequence

Monazite ages from the Chickies Quartzite (Zch, Figs. 15b and 16) suggest that the effects of Taconian orogenesis: 1) were not responsible for Paleozoic alteration (chlorite rims on garnet, albite + epidote + muscovite replacing plagioclase + K-feldspar, rutile + titanite rims on ilmenite) of former amphibolite- or granulite-facies mineral assemblages in HBU samples; 2) produced little metamorphic recrystallization of rocks in the Chester Valley Sequence. The Taconian orogeny transported the allocthonous Honey Brook Upland and Chester Valley sequence westward to or near their present-day positions (Mackin, 1962; McKinstry, 1961; Freedman et al., 1964; Crawford and Hoersch, 1984, 1988; Faill, 1997), but the position of the Honey Brook Upland and the Chester Valley Sequence in the highest structural level of the Reading Megnappe System (MacLachlan, 1994; Faill, 1997) resulted in thrust sheet transport (Herman et al., 1994) rather than the extensive recumbent folding and tectonization present in the lower parts of the nappe sequence (Wise, 1970), and, consequently, a lack of pervasive deformation. Moreover, the Honey Brook Upland and Chester Valley Sequence were a greater distance from the Taconic metamorphic core, and not significantly overridden by the Octoraro Basin thrust sheets (e.g., Embreeville thrust), resulting in a lesser degree of burial metamorphism than that experienced within the Avondale and West Chester Massifs. The two distinct monazite age domains in the Chickies Quartzite (378 ± 28 and

272 ± 44 Ma) suggest that both Acadian and Alleghanian orogenesis produced distinct metamorphic signatures within the Chester Valley Sequence.

The major components of Alleghanian deformation in the Pennsylvania Piedmont are early, low-angle thrust faults trending ENE with NW transport, and later dextral transform faults and shear zones (Valentino, 1999; Valentino et al., 1994, 1999); the Honey Brook Upland is in the upper plate of the Oregon (Mechanicsville) thrust (MacLachlan, 1994; Faill, 1998), and the Chester Valley Sequence is bounded on the south by the South Valley Shear zone (MacLachlan, 1994). The 272 ± 44 Ma monazite age domain in the Chickies Quartzite apparently records a metamorphic response to either thrusting or transpressional tectonism during the Alleghanian orogeny. However, evidence for low-grade Acadian metamorphism of the Chester Valley Sequence is recorded by the 378 ± 28 Ma monazite age domain in the Chickies Quartzite. The Tucquan Antiform and Mine Ridge (to the SW of the Honey Brook Upland, Fig. 1) contain Taconic-style subhorizontal cleavage and isoclinal folding cross-cut by sub-vertical slip surfaces and re-folded into upright, open regional-scale folds (Freedman et al., 1964; Wise, 1970). Debate continues as to whether these post-Taconic structures result from Acadian or Alleghanian orogenesis (e.g, Faill, 1998), but $^{40}K/^{39}Ar$ mica cooling ages from similar structures in Maryland (Lapham and Basset, 1964) range between 360 and 320 Ma, allowing for 20–60 m.y. between low-grade Devonian metamorphism of the Chester Valley Sequence and cooling through Ar closure temperatures in the Mississippian (e.g., Krol et al., 1999). If two Paleozoic metamorphic events are recorded by monazite growth in the Chickies Quartzite, both are similar in their low metamorphic grade.

The tectonic emplacement of the HBU and CVS, begun in the Ordovician, progressed through the late Paleozoic as a result of both northwest-directed thrusting and dextral transpression. Transport estimates due to Alleghanian thrusting are on the order of 10s of km (Faill, 1998), and estimated movement along Alleghanian transpressional faults or shear zones exposed in the PA piedmont (e.g., Lancaster Valley shear zone, Huntington Valley shear zone, Pleasant Grove shear zone) range from 4–7 km (Krol et al., 1990) to 150+ km (Valentino et al., 1994). A reversed-facies-sequence of slope deposits south of the Honey Brook Upland overlying shelf deposits south of the Mine Ridge suggests a ~40 km dextral displacement of Mine Ridge from south of the Honey Brook Upland (MacLachlan, 1994).

Black slates in the Peach Bottom slate belt (~5 km NW of the westernmost group of ultramafic rocks, Fig. 1b) contain foliation formed during dextral transpression. These slates yield K–Ar whole rock ages of 279 ± 6 and 276 ± 6 Ma (Faill and Smith, 1994). This similarity of this age to younger monazite ages in the Chickies Quartzite suggests that younger Chickies monazites may have formed during the transpressional phase of Alleghanian metamorphism.

9.4. Non-correspondence of monazite ages in HBU meta-plutonic and meta-volcanic units

A notable result is the non-correspondence of monazite ages in the meta-plutonic (Yhfg; 710, 585 Ma) and meta-volcaniclastic samples (Yhga; 1020, 965, 870 Ma) from the Honey Brook Upland, and the lack of Paleozoic monazite ages in either set of samples, given that Paleozoic monazite is present in the Chickies Quartzite. Monazite inclusions in apatite in HBU gneisses are too Pb-poor to be dated by EMPA. This observation implies that such monazite inclusions are Paleozoic; a 1.0 Ga monazite with 0.3 wt.% Th and 0.1 wt.% U will contain ~300 ppm total Pb, which is well above the detectability limit at operating conditions used in this study (Pyle et al., 2005).

One factor that may be responsible for the difference in monazite ages in the different Upland gneiss units is bulk composition. It has been demonstrated that particular bulk composition factors such as Ca/Al ratio (Wing et al., 2003) and Fe/(Fe+Mg) (Fitzsimons et al., 2005) control monazite paragenesis by: a) stabilizing other REE-bearing accessory phases such as allanite (Wing et al., 2003), or; b) controlling major-phase reaction history, which in turn controls accessory phase paragenesis if the reacting (or non-reacting) major phases preferentially fractionate P, REE and Y (Fitzsimons et al., 2005). Bulk rock analysis of "granuilite-facies" gneiss (Yhfg) and "amphibolite-facies" gneiss (Yhga) (Crawford and Hoersch, 1984) shows that, on average, the units differ slightly in whole-rock Ca/Al ratio (0.18 (Yhfg) vs. 0.22 (Yhga)) and significantly in whole-rock Fe/(Fe+Mg) (0.73 vs. 0.47), Fe^{3+}/Fe^{2+} (0.25 vs. 0.17) and Al/Ca+Na+K (i.e., peraluminosity) (1.01 vs. 1.11).

Bulk composition of Yhfg promoted allanite as the initial REE-bearing phase, whereas monazite was the initial REE-bearing phase in Yhga. The two samples also encountered different fluid compositions during their respective evolutions, as indicated by the presence of calcite in Yhfg and its absence in Yhga. The growth of significant garnet in Yhga (a more Fe-rich bulk composition), and concomitant fractionation of P, Y and MREE-HREE contributed to suppression of later

(Paleozoic) monazite growth. In the garnet-free metaplutonic rocks, reaction of allanite and REE-bearing apatite induced limited monazite growth as shown above. These monazite growth events may have been Neoproterozoic (as are monazite inclusions in coronas around Opx), or Paleozoic, and thus likely correlating to the event or events that produced greenschist retrogression of garnet, ilmenite, and calcic plagioclase.

9.5. Interpretations based on sparse data sets

The data presented in this paper represents four samples from three different lithologic units. Although the samples are representative of their respective lithologic units, the *T–t* data extracted from each sample may not be representative of the entire terrane, and thus sample-specific interpretations may not extend to the Honey Brook Upland or the Chester Valley Sequence as a whole.

In this case, a sparse data set can be evaluated only by: 1) comparison to other *T–t* data from the same lithologic units, or; 2) comparison to *T–t* data from other terranes where temporal and tectonic correlation is a reasonable assumption. The former comparison is more robust, but quantitative *T–t* data for the Honey Brook Upland and Chester Valley Sequence are limited. For the latter evaluation, the comparable terranes are the Adirondacks and other Grenville inliers within the central Appalachians.

With regard to comparable temperature data: 1) 2-pyroxene thermometry for sample Yhfg1 yields emplacement temperatures (900–950 °C) similar to reintegrated two-pyroxene thermometry estimates from Adirondack meta-mangerite (Nabelek et al., 1987); 2) estimated temperatures for the Opx–Cum reaction in Yhfg1 (730–740 °C) are consistent with C-isotope exchange thermometry estimates (750 ± 40 °C) for rocks from the same unit (Crawford and Valley, 1990); 3) peak monazite (core domain)–xenotime equilibration temperatures for sample Yhga (700 °C) are indistinguishable from C-isotope exchange thermometry estimates (680 ± 40 °C) for rocks from the same unit (Crawford and Valley, 1990); 4) the upper limit of monazite–xenotime thermometry estimates for sample Zch1 (Chickies Quartzite) is not inconsistent with the lower limit of temperature conditions for grennschist-facies metamorphism.

With regard to comparable age data: 1) ~1020 and ~970 Ma monazite ages from sample Yhga are not inconsistent with similar ages from proximal Grenville terranes, such as ~1020 Ma metamorphic zircon rims in felsic members of the Baltimore Gneiss (Aleinikoff et al., 2004) and a terminal Grenville metamorphic age of 993 ± 8 Ma from zircon in hornblende gneiss from Western Connecticut (Walsh et al., 2004); 2) The ~870 Ma age for inferred hydrothermal monazite (sample Yhga) does not contradict the biotite $^{40}Ar/^{39}Ar$ cooling age of 850 Ma (Sutter et al., 1980) for the Honey Brook Upland; 3) The 583 ± 92 Ma age for alteration monazite in Yhfg correlates with known igneous activity in the Reading Prong (602 ± 2 Ma felsite; Smith, 2003) and the Honey Brook Upland (~570 Ma Catoctin-affinity diabase). This late Proterozoic thermal event may also be recorded by a 567 Ma biotite-whole rock Rb–Sr cooling age from a HBU sample correlative with Yhga (Kohn et al., 1993); 4) Regarding ~380 and ~270 Ma ages for monazite from sample Zch (Chickies Quartzite); a) The older monazite ages are consistent with Acadian metamorphic ages to the south of the Chester Valley Sequence, and do not contradict mica K–Ar cooling ages of 360–320 Ma (Lapham and Bassett, 1964); b) The younger monazite ages are consistent with a K–Ar whole rock age of 279–276 Ma for slates of the Peach Bottom Slate Belt (Faill and Smith), and both are correlated with formation during Alleghanian transpression.

The above analysis demonstrates that the *T–t* data from the HBU and CVS agrees, within analytical uncertainty, with directly comparable *T–t* data, and are not contradicted by comparable cooling ages. Moreover, comparisons between the HBU and correlative Grenville terranes support the existence of regionally significant 1020–970 Ma metamorphism in what is now the central Appalachians. However, terrane-wide (i.e., HBU and CVS) interpretations will require collection of more data.

10. Conclusion

Phosphate accessory phases in gneisses of the Honey Brook Upland, and metasediments of the overlying Chester Valley Sequence, record high-grade Grenville-age metamorphism, late Proterozoic thermal disturbance, and low-grade Paleozoic metamorphism, unlike higher-grade Paleozoic metamorphism in the terranes south of the Chester Valley. Paleozoic metamorphism of the CVS and the HBU gneisses appears to be largely related to Acadian and Alleghanian orogenesis. This also contrasts with terranes to the south of the Chester Valley, where Acadian and older metamorphic effects dominate.

This study sheds light on differences in the metamorphic evolution of the Honey Brook Upland and Chester Valley Sequence, relative to that of the Avondale–West Chester Massif and Glenarm Series. Further

elucidation of these differences will be aided by: 1) obtaining U/Pb ages of primary zircon or allanite in meta-igneous HBU rocks; 2) sampling and dating of late Proterozoic metavolcanics at the base of the Chickies formation, and; 3) identification and dating of monazite in the pelitic sequences of continental slope-facies Conestoga Formation. Attaining this age data will also place further constraints on the Proterozoic evolution of the Honey Brook Upland in the larger context of overall Grenvillian or genesis.

Acknowledgements

F. Spear and L. Storm are acknowledged for coding computer software to perform Monte Carlo simulations and MSWD statistical deconvolutions of age data. H. Bosbyshell and G. Blackmer are thanked for sharing their enthusiasm in continued studies of the Pennsylvania Piedmont. Conversations with R. Smith and L. Marquez helped in formulation of the discussion. J. Baldwin is thanked for her aid (and patience) as co-editor of this volume. D. Harlov and M.L. Crawford are thanked for their constructive reviews, which considerably improved an earlier version of the manuscript.

Appendix A. Supplementary data

Supplementary data associated with this article can be found, in the online version, at doi:10.1016/j.lithos.2005.08.010.

References

Alcock, J., Wagner, M.E., 1995. Metamorphic discontinuities of the Pennsylvania–Delaware Piedmont: evidence for early Paleozoic assembly. Canadian Journal of Earth Sciences 32, 686–698.

Aleinikoff, J.N., Horton, J.W.J., Walter, M., 1996. Middle Proterozoic age for the Montpelier Anorthosite, Goochland terrane, eastern Piedmont, Virginia. Geological Society of America Bulletin 108, 1481–1491.

Aleinikoff, J.N., Horton, J.W.J., Drake Jr., A.A., Wintsch, R.P., Fanning, C.M., Yi, K., 2004. Deciphering multiple Mesoproterozoic and Paleozoic events recorded in zircon and titanite from the Baltimore Gneiss, Maryland: SEM imaging, SHRIMP U–Pb geochronology, and EMP analysis. In: Tollo, R.P., Corriveau, L., McLelland, J.M., Bartholomew, M.J. (Eds.), Proterozoic Tectonic Evolution of the Grenville Orogen in North America, Geological Society of America Memoir, vol. 197. Geological Society of America, Boulder, pp. 411–434.

Amli, R., 1975. Mineralogy and rare earth geochemistry of apatite and xenotime from the Gloserheia granite pegmatite, Froland, southern Norway. American Mineralogist 60, 607–620.

Bascom, F., 1905. Piedmont district of Pennsylvania. Geological Society of America Bulletin 16, 289–328.

Bascom, F., Stose, G.W., 1932. Description of the Coatesville and West Chester quadrangles, Pennsylvania–Delaware. United States Geological Survey Geological Atlas of the United States Folio, vol. 223. 15 pp.

Bascom, F., Stose, G.W., 1938. Geology and mineral resources of the Honeybrook and Phoenixville Quadrangles. U.S. Geological Survey Bulletin 891, 1–145.

Bascom, F., Clark, B., Darton, N.H., Kummel, H.B., Salisbury, R.D., Miller, B.L., Knapp, G.N., 1909. Folio, vol. 162. U.S. Geological Survey Geological Atlas of the U.S., Philadelphia Folio.

Bea, F., 1996. Residence of REE, Y, Th and U in granites and crustal protoliths; implications for the chemistry of crustal melts. Journal of Petrology 37, 521–552.

Bea, F., Montero, P., 1999. Behavior of accessory phases and redistribution of Zr, REE, Y, Th, and U during metamorphism and partial melting of metapelites in the lower crust: an example from the Kinzigite Formation of Ivrea–Verbano, NW Italy. Geochimica et Cosmochimica Acta 63, 1133–1153.

Berg, T.M., Edmunds, W.E., Geyer, A.R., Glover, A.D., Hoskins, D.M., MacLachlan, D.B., Root, S.I., Sevon, W.D., Socolow, A.A., 1980. Geologic Map of Pennsylvania. Pennsylvania Department of Environmental Resources, Harrisburg.

Bliss, E.F., Jonas, A.I., 1916. Relation of the Wissahickon mica gneiss to the Shenandoah limestone and the Octoraro schist of the Doe Run and Avondale region, Chester County, PA. United States Geological Survey Professional Paper 98, 9–34.

Broska, I., Petrik, I., Williams, C.T., 2000. Coexisting monazite and allanite in peraluminous granitoids of the Tribec Mountains, western Carpathians. American Mineralogist 85, 22–32.

Cloos, E., Hietanen, A.M., 1941. Geology of the "Martic Overthrust" and the Glenarm Series in Pennsylvania and Maryland (Geological Society of America Special Paper). Geological Society of America, Boulder, CO. 207 pp.

Crawford, M.L., Crawford, W.A., 1980. Metamorphic and tectonic history of the Pennsylvania Piedmont. Journal of the Geological Society (London) 137, 311–320.

Crawford, W.A., Hoersch, A.L., 1984. The geology of the Honey Brook Upland, southeastern Pennsylvania. In: Bartholomew, M.J. (Ed.), The Grenville Event in the Appalachians and Related Topics, Geological Society of America Special Paper, vol. 194. Geological Society of America, Boulder, CO, pp. 111–125.

Crawford, W.A., Hoersch, A.L., 1988. The Mine Ridge of the southeast Pennsylvania Piedmont. Northeastern Geology 10, 181–194.

Crawford, W.A., Valley, J.W., 1990. Origin of graphite in the Pickering Gneiss and the Franklin Marble, Honey Brook Upland, Pennsylvania Piedmont. Geological Society of America Bulletin 102, 807–811.

Crawford, W.A., Roblen, P.G., Kalmbach, J.H., 1971. The Honey Brook anorthosite. American Journal of Science 271, 333–349.

Crawford, M.L., Crawford, W.A., Hoersch, A.L., Wagner, M.E., 1999. Selected rocks of the Piedmont upland. In: Schulze, C.H. (Ed.), The Geology of Pennsylvania. Pennsylvania Geological Survey, Harrisburg, pp. 26–35.

Demmon, F.E., 1977. Investigations of the origins and metamorphic history of Precambrian gneisses, Downingtown 7.5′ quadrangle, southeastern Pennsylvania (MA Thesis), Bryn Mawr College, 71 pp.

Dill, J.A.M., 1974. Inferred metamorphic grade of ten marble and calc-silicate assemblages from Pennsylvania and New Jersey (BA thesis (honors)), Bryn Mawr College, 60 pp.

Faill, R.T., 1997. A geologic history of the north-central Appalachians. Part 1. Orogenesis from the Mesoproterozoic through the Taconic Orogeny. American Journal of Science 297, 551–619.

Faill, R.T., 1998. A geologic history of the north-central Appalachians. Part 3, The Alleghany orogeny. American Journal of Science 298, 131–179.

Faill, R.T., Smith, R.C. II, 1994. Stop 14. Peach bottom section at the Susquehanna River, Table 13-C. In: Faill II, R.T., Sevon, W.D. (Eds.), Various Aspects of Piedmont Geology in Lancaster and Chester Counties, Pennsylvania, Guidebook, Annual Field Conference of Pennsylvania Geologists, vol. 59, p. 185.

Faure, G., 1986. Principles of Isotope Geology, Second edition John Wiley & Sons, New York. 589 pp.

Fitzsimons, I.C.W., Kinney, P.D., Wetherly, S., Hollingsworth, A., 2005. Bulk chemical control on metamorphic monazite growth in pelitic schists and implications for U–Pb age data. Journal of Metamorphic Geology 23, 261–277.

Fonarev, V.I., Korolkov, G.J., 1980. The assemblage orthopyroxene+cummingtonite+quartz. The low-temperature stability limit. Contributions to Mineralogy and Petrology 73, 413–420.

Förster, H.-J., 1998. The chemical composition of REE–Y–Th–U-rich accessory minerals in peraluminous granites of the Erzgebirge–Fichtelgebirge region, Germany, part I: the monazite-(Ce)-brabantite solid solution series. American Mineralogist 83, 259–272.

Foster, G., Parrish, R.R., Horstwood, M.S.A., Chenery, S., Pyle, J., Gibson, H.D., 2004. The generation of P–T–t prograde points and paths; a textural, compositional, and chronological study of metamorphic monazite. Earth and Planetary Science Letters 228, 125–142.

Freedman, J., Wise, D., Bentley, R., 1964. Pattern of folded folds in the Appalachian Piedmont along Susquehanna River. Geological Society of America Bulletin 75, 621–638.

Gibson, H.D., Carr, S.D., Brown, R.L., Hamilton, M.A., 2004. Correlations between chemical and age domains in monazite, and metamorphic reactions involving major pelitic phases: an integration of ID-TIMS and SHRIMP geochronology with Y–Th–U X-ray mapping. Chemical Geology 211, 237–260.

Gratz, R., Heinrich, W., 1997. Monazite–xenotime thermometry: experimental calibration of the miscibility gap in the system $CePO_4$–YPO_4. American Mineralogist 82, 772–780.

Grauert, B., Crawford, M.L., Wagner, M.E., 1973. U–Pb isotopic analysis of zircons from granulite and amphibolite facies rocks of the West Chester Prong and the Avondale anticline, southeastern Pennsylvania. Yearbook of the Carnegie Institute of Washington, vol. 72, pp. 290–293.

Grove, M., Harrison, T.M., 1996. 40Ar* diffusion in Fe-rich biotite. American Mineralogist 81, 940–951.

Harlov, D.E., Forster, H.-J., 2003. Fluid-induced nucleation of (Y+REE)–phosphate minerals within apatite: nature and experiment. Part II. Fluorapatite. American Mineralogist 88, 1209–1229.

Harlov, D.E., Forster, H.-J., Nijland, T., 2002. Fluid-induced nucleation of (Y+REE)–phosphate minerals within apatite: nature and experiment. Part I. Chlorapatite. American Mineralogist 87, 245–261.

Harrison, T.M., 1981. Diffusion of ^{40}Ar in hornblende. Contributions to Mineralogy and Petrology 78, 324–331.

Harrison, T.M., McKeegan, K.D., LeFort, P., 1995. Detection of inherited monazite in the Manaslu leucogranite by (super 208) Pb/(super 232) Th ion microprobe dating; crystallization age and tectonic implications. Chemical Geology 133, 271–282.

Hecht, L., Cuney, M., 2000. Hydrothermal alteration of monazite in the Precambrian crystalline basement of the Athabasca Basin (Saskatchewan, Canada): implications for the formation of unconformity-related uranium deposits. Mineralium Deposita 35, 791–795.

Heinrich, W., Andrehs, G., Franz, G., 1997. Monazite–xenotime miscibility gap thermometry; 1, an empirical calibration. Journal of Metamorphic Geology 15, 3–16.

Herman, G.C., Monteverde, D.H., Volkert, R.A., Houghton, H.F., Parker, R.A., Drake, A.A. Jr., Dalton, R.A., 1994. Cross Sections of the Valley and Ridge, Highlands, and Piedmont Provinces, Northern and Central Bedrock Sheets, New Jersey. Open-file Report - United States Geological Survey. 45 pp.

Huntsman, J.R., 1975. Crystalline rocks of the Wagontown 7.5′ quadrangle (MA Thesis), Bryn Mawr College, 69 pp.

Irvine, T.N., Baragar, W.R.A., 1971. A guide to the chemical classification of the common volcanic rocks. Canadian Journal of Earth Sciences 8, 523–548.

Kaufman, M.E., 1999. Eocambrian, Cambrian, and transition to Ordovician. In: Schulze II, C.H. (Ed.), The Geology of Pennsylvania. Pennsylvania Geological Survey, Harrisburg, pp. 58–73.

Knopf, E.B., Jonas, A.I., 1923. Stratigraphy of the crystalline schists of Pennsylvania and Maryland. American Journal of Science 5, 40–62.

Knopf, E.B., Jonas, A.I., 1929. Geology of the McCalls Ferry-Quarryville district, Pennsylvania. U.S. Geological Survey Bulletin 799 (156 pp.).

Kohn, B.P., Wagner, M.E., Lutz, T.M., Organist, G., 1993. Anomalous Mesozoic thermal regime, central Appalachian Piedmont: evidence from sphene and zircon fission-track dating. Journal of Geology 101, 779–794.

Kretz, R., 1983. Symbols for rock-forming minerals. American Mineralogist 68, 277–279.

Krol, M.A., Onsach, C.M., Muller, P.D., 1990. Kinematic analysis of the Pleasant Grove shear zone, eastern Maryland Piedmont. Abstracts with Programs - Geological Society of America 22, 28.

Krol, M.A., Muller, P.D., Idelman, B.D., 1999. Late Paleozoic deformation within the Pleasant Grove shear zone, Maryland: results from $^{40}Ar/^{39}Ar$ dating of white mica. In: Valentino, D.W., Gates, A.E. (Eds.), The Mid-Atlantic Piedmont: Tectonic Missing Link of the Appalachians, Geological Society Paper of America Special Paper, vol. 330. Geological Society of America, Boulder, CO, pp. 93–111.

Lapham, D.M., Basset, W.A., 1964. K–Ar dating of rocks and tectonic events in the Piedmont of southeastern Pennsylvania. Geological Society of America Bulletin 75, 661–668.

Lindsley, D.H., Andersen, D.J., 1983. A two-pyroxene thermometer. Proceedings of the Thirteenth Lunar and Planetary Science Conference, Part 2, Journal of Geophysical Research, pp. A887–A906.

Mackin, J.H., 1962. Structure of the Glenarm series in Chester County, Pennsylvania. Geological Society of America Bulletin 73, 403–409.

MacLachlan, D.B., 1994. Some aspects of the lower Paleozoic Laurentian margin and slope in southeastern Pennsylvania. In: Faill, R.T., Sevon, W.D. (Eds.), Various Aspects of Piedmont Geology in Lancaster and Chester Counties, Pennsylvania, Guidebook, Annual Field Conference of Pennsylvania Geologists, vol. 59, pp. 3–24.

McKinstry, H.E., 1961. Structure of the Glenarm Series in Chester County, Pennsylvania. Geological Society of America Bulletin 72, 557–578.

McLelland, J.M., Bickford, M.E., Hill, B.M., Clechenko, C.C., Valley, J.W., Hamilton, M.A., 2004. Direct dating of Adirondack massif anorthosite by U–Pb SHRIMP analysis of igneous zircon: implications for AMCG complexes. Geological Society of America Bulletin 116, 1299–1317.

Meisler, H., Becher, A.E., 1968. Carbonate rocks of Cambrian and Ordovician age in the Lancaster Quadrangle, Pennsylvania. U.S. Geological Survey Bulletin 1254G (14 pp.).

Miller, B.L., 1912. The geology of the graphite deposits of Pennsylvania. Economic Geology 7, 762–777.

Montel, J.-M., Foret, S., Veschanbre, M., Nicollet, C., Provost, A., 1996. Electron microprobe dating of monazite. Chemical Geology 131, 37–53.

Nabelek, P.I., Lindsley, D.H., Bohlen, S.R., 1987. Experimental examination of two-pyroxene graphical thermometers using natural pyroxenes with applications to metaigneous pyroxenes from the Adirondack Mountains, New York. Contributions to Mineralogy and Petrology 97, 66–71.

O'Neill, B.J., 1952. Geology of the anorthosite massif in Chester County, PA (MS Thesis). M.S. Thesis, California Institute of Technology, 35 pp.

Organist, G., 1978. Organist, G. (1978). A study of the Honey Brook anorthosite country rock contact (MA Thesis), Bryn Mawr College, 30 pp.

Parks, E.J., 1993. Crustal Evolution of Grenville terranes in the central and southern Appalachians; the Pb isotope perspective for Grenville tectonics (MS thesis), Virginia Polytechnic Institute and State University, 71 pp.

Parrish, R.R., 1990. U–Pb dating of monazite and its application to geological problems. Canadian Journal of Earth Sciences 27, 1431–1450.

Peiffert, C., Nguyen-Trung, C., Cuney, M., 1996. Uranium in granitic magmas. 2. Experimental determination of uranium solubility and fluid-melt partition coefficients in the uranium oxide–haplogranite–H2O–NaX (X=Cl, F) system at 770 degrees C, 2 kbar. Geochimica et Cosmochimica Acta 60, 1515–1529.

Poitrasson, F., Chenery, S., Sheperd, T.J., 2000. Electron microprobe and LA–ICP–MS study of monazite hydrothermal alteration: implications for U–Pb–Th geochronology and nuclear ceramics. Geochimica et Cosmochimica Acta 64, 3283–3297.

Postel, A.W., 1951. Problems of the Pre-Cambrian in Phoenixville and Honeybrook quadrangles, Chester County, Pennsylvania. Pennsylvania Academy of Science Transactions 25, 113–119.

Pupa, D.M., 1988. Crystalline rocks of the Honey Brook 7.5′ quadrangle, southeastern Pennsylvania (MA thesis), Bryn Mawr College, 76 pp.

Pyle, J.M., 2001. Distribution of select trace elements in pelitic metamorphic rocks: pressure, temperature, mineral assemblage, and reaction-history controls (PhD Thesis), Rensselaer Polytechnic Institute, 352 pp.

Pyle, J.M., Spear, F.S., 1999. Yttrium zoning in garnet: coupling of major and accessory phases during metamorphic reactions. Geological Materials Research 1 (6), 1–49.

Pyle, J.M., Spear, F.S., 2000. An empirical garnet (YAG) — xenotime thermometer. Contributions to Mineralogy and Petrology 138, 51–58.

Pyle, J.M., Spear, F.S., 2003. Four generations of accessory phase growth in low-pressure migmatites from SW New Hampshire, USA. American Mineralogist 88, 338–351.

Pyle, J.M., Spear, F.S., Rudnick, R.L., McDonough, W.F., 2001. Monazite–xenotime–garnet equilibrium in metapelites and a new garnet–monazite thermometer. Journal of Petrology 42, 2083–2107.

Pyle, J.M., Spear, F.S., Wark, D.A., Daniel, C.G., Storm, L.C., 2005. Contributions to precision and accuracy of monazite microprobe ages. American Mineralogist 90, 547–577.

Rankin, D.W., 1976. Appalachian salients and recesses; late Precambrian continental breakup and the opening of the Iapetus Ocean. Journal of Geophysical Research 81, 5605–5619.

Robelen, P.G., 1968. The petrology of the Honeybrook anorthosite, Chester County, Pennsylvania (MA Thesis), Bryn Mawr College, 30 pp.

Sandford, R.S., Lamb, F.D., 1949. Investigation of the Benjamin Franklin Graphite Mine (Government Owned) and the Just Graphite Mine, Chester County, Pennsylvania. U.S. Bureau of Mines Report of Investigation, vol. 4530. 17 pp.

Seydoux-Guillaume, A.-M., Wirth, R., Heinrich, W., Montel, J.-M., 2002. Experimental determination of thorium partitioning between monazite and xenotime using analytical electron microscopy and X-ray diffraction Rietveld analysis. European Journal of Mineralogy 14, 869–878.

Sinha, A.K., Hogan, J.P., Parks, J., 1996. Lead isotope mapping of crustal reservoirs within the Grenville Superterrane: I. Central and southern Appalachians. In: Basu, A., Hart, S. (Eds.), Earth Processes: Reading the Isotopic Code, American Geophysical Union Geophysical Monograph, vol. 95, pp. 293–304.

Sloto, R.A., 1994. Geology, hydrology, and ground water quality of Chester County, Pennsylvania. Chester County water resources authority. Water Resource Report 2 (127 pp.).

Smith, R.C. II, 2003. Late Neoproterozoic felsite (602.3 ± 2 Ma) and associated metadiabase dikes in the Reading Prong, Pennsylvania, and rifting of Laurentia. Northeastern Geology and Environmental Sciences, vol. 25, pp. 175–185.

Smith, R.C. II, Barnes, J.H., 1994. Geochemistry and geology of metabasalt in southeastern Pennsylvania and adjacent Maryland. In: Faill II, R.T., Sevon, W.D. (Eds.), Various aspects of Piedmont geology in Lancaster and Chester Counties, Pennsylvania, Guidebook, Annual Field Conference of Pennsylvania Geologists, vol. 59, pp. 45–72.

Spear, F.S., Kohn, M.J., 1996. Trace element zoning as a monitor of crustal melting. Geology 24, 1099–1102.

Spear, F.S., Markussen, J.C., 1997. Mineral zoning, P–T–X–M phase relations, and metamorphic evolution of some Adirondack granulites, New York. Journal of Petrology 38, 757–783.

Stormer, J.C., Pierson, M.L., Tacker, R.C., 1993. Variation of F and Cl X-ray intensity due to anisotropic diffusion in apatite during electron microprobe analysis. American Mineralogist 78, 641–648.

Stose, G.W., Jonas, A.I., 1922. The lower Paleozoic section of southeastern Pennsylvania. Washington Academy of Science Journal 12, 358–366.

Stose, G.W., Jonas, A.I., 1923. Ordovician overlap in the Piedmont province of Pennsylvania and Maryland. Geological Society of America Bulletin 34, 507–524.

Stose, G.W., Jonas, A.I., 1927. Ordovician shale and associated lava in southeastern Pennsylvania. Geological Society of America Bulletin 38, 505–536.

Streckeisen, A., 1976. To each plutonic rock its proper name. Earth-Science Reviews 12, 1–33.

Sutter, J.F., Crawford, M.L., Crawford, W.A., 1980. $^{40}Ar/^{39}Ar$ age spectra of coexisting hornblende and biotite from the Piedmont of Pennsylvania: their bearing on the metamorphic and tectonic history. Abstracts with Programs - Geological Society of America 12, 85.

Thomann, W.F., 1977. Igneous and metamorphic petrology of the Honey Brook Uplands in the Elverson, Pottstown, and Phoenixville quadrangles, southeastern Pennsylvania (MA thesis), Bryn Mawr College, 65 pp.

Thompson, A.B., Tracy, R.J., 1979. Model-systems for anatexis of pelitic rocks; II, Facies series melting and reactions in the system $CaO–KAlO_2NaAlO_2–Al_2O_3–SiO_2–H_2O$. Contributions to Mineralogy and Petrology 70, 429–438.

Valentino, D.W., 1999. Late Paleozoic dextral transpression in the crystalline core of the Pennsylvania reentrant. In: Valentino, D.W., Gates, A.E. (Eds.), The Mid-Atlantic Piedmont: Tectonic Missing Link of the Appalachians, Geological Society Paper of America Special Paper, vol. 330. Geological Society of America, Boulder, CO, pp. 59–71.

Valentino, D.W., Gates, A.E., Glover, L.G. III, 1994. Late Paleozoic transcurrent tectonic assembly of the central Appalachian Piedmont. Tectonics 13, 110–126.

Valentino, D.W., Valentino, R.W., Lamport, B.J., 1999. Interaction between Paleozoic strike-slip and thrust shear zones in the Philadelphia structural block, central Appalachian Piedmont. In: Valentino II, D.W., Gates, A.E. (Eds.), The Mid-Atlantic Piedmont: Tectonic Missing Link of the Appalachians, Geological Society Paper of America Special Paper, vol. 330. Geological Society of America, Boulder, CO, pp. 29–39.

Valley, J.W., O'Neil, J.R., 1981. $^{13}C/^{12}C$ exchange between calcite and graphite: a possible thermometer in Grenville marbles. Geochemica et Cosmochimica Acta 45, 411–419.

Wagner, M.E., Crawford, M.L., 1975. Polymetamorphism of the Precambrian Baltimore Gneiss in Southeastern Pennsylvania. American Journal of Science 275, 653–682.

Walsh, G.J., Aleinikoff, J.N., Fanning, C.M., 2004. U–Pb geochronology and evolution of Mesoproterozoic basement rocks, western Connecticut. In: Tollo, R.P., Corriveau, L., McLelland, J.M., Bartholomew, M.J. (Eds.), Proterozoic Tectonic Evolution of the Grenville Orogen in North America, Geological Society of America Memoir, vol. 197. Geological Society of America, Boulder, pp. 729–753.

Waraska, I.R., 1952. The petrology and structural geology of the Pre-Cambrian igneous rocks near Wallace, Chester County, Pennsylvania (M.A. thesis), Bryn Mawr College, 17 pp.

Wendt, I., Carl, C., 1991. The statistical distribution of the mean squared weighted deviation. Chemical Geology. Isotope Science Section 86, 275–285.

Wing, B.A., Ferry, J.M., Harrison, T.M., 2003. Prograde destruction and formation of monazite and allanite during contact and regional metamorphism of pelites; petrology and geochemistry. Contributions to Mineralogy and Petrology 145, 228–250.

Wise, D.U., 1970. Multiple deformation, geosynclinal transitions, and the Martic problem in Pennsylvania. In: Fisher, G.W., Pettijohn, F.J., Reed Jr., J.C., Weaver, K.N. (Eds.), Studies of Appalachian Geology: Central and Southern. Wiley Interscience, New York, pp. 317–334.